

The re-markable 21-cm power spectrum I: Probing the H I distribution in the post-reionization era using marked statistics

**Mohd Kamran,^a Martin Sahlén,^a Debanjan Sarkar,^{b,c,d}
Suman Majumdar^{e,f}**

^aTheoretical Astrophysics, Department of Physics and Astronomy, Uppsala University, Box 516, 751 20 Uppsala, Sweden

^bDepartment of Physics and Trottier Space Institute, McGill University, QC H3A 2T8, Canada

^cCiela—Montreal Institute for Astrophysical Data Analysis and Machine Learning, QC H2V 0B3, Canada

^dDepartment of Physics, Ben-Gurion University of the Negev, Be'er Sheva 84105, Israel

^eDepartment of Astronomy, Astrophysics & Space Engineering, Indian Institute of Technology Indore, Indore 453552, India

^fDepartment of Physics, Blackett Laboratory, Imperial College, London SW7 2AZ, U. K.

E-mail: kamranmohd080@gmail.com

Abstract. The neutral hydrogen (HI) power spectrum, measured from intensity fluctuations in the 21-cm background, offers insights into the large-scale structures (LSS) of our Universe in the post-reionization era (redshift $z < 6$). A significant amount of HI is expected to reside in low- and intermediate-density environments, but the power spectrum mainly captures information from high-density regions. To more fully extract the information contained in the HI field, we investigate the use of a marked power spectrum statistic. Here, the power spectrum is effectively re-weighted using a non-linear mark function which depends on the smoothed local density, such that low- or high-density regions are up- or down-weighted. This approach may also capture information on some higher-order statistical moments of the field. We model the HI distribution using semi-numerical simulations and for the first time study the marked HI power spectrum, across $1 \leq z \leq 5$.

Our analysis indicates that there is considerable evolution of the HI field during the post-reionization era. Over a wide range of length scales (comoving wave numbers $0.05 \leq k \leq 1.0 \text{ Mpc}^{-1}$) we expectedly find that the HI evolves slowly at early times, but more rapidly at late times. This evolution is not well-captured by the power spectrum of the standard (unmarked) HI field. We also study how the evolution of the HI field depends on the chosen smoothing scale for the mark, and how this affects the marked power spectrum.

We conclude that the information about the HI content at low and intermediate densities is important for a correct and consistent analysis of HI content and evolution based on the 21-cm background. The marked power spectrum can thus provide a less biased statistic for parameter constraints than the normal power spectrum.

Keywords: cosmology: theory, large scale structures, diffuse radiation—methods: statistical

Contents

1	Introduction	1
2	Simulating the H_I distribution in the post-reionization era	4
2.1	<i>N</i> -body simulation	4
2.2	Finding FoF halos	4
2.3	Simulating H _I using $M_{\text{h}} - M_{\text{HI}}$ relation	4
3	Formalism of marked statistics	7
3.1	The marked correlation function	7
3.2	The choices of the mark	8
4	Results	9
4.1	The Fourier mode (k) dependence of the marked H _I power spectra (MPS)	12
4.1.1	MPS for p_{hd}	12
4.1.2	MPS for p_{ld1}	15
4.2	The smoothing scale (R) dependence of the MPS	16
4.2.1	MPS for p_{hd}	17
4.2.2	MPS for p_{ld1}	18
5	Summary and discussions	19
6	Acknowledgements	21
A	Appendix	22
A.1	A different functional form of the mark	22
A.2	The impact of the parameter ρ_* on the marked power spectra	22

1 Introduction

The 21-cm radiation arising from the hyperfine transition within the ground state of the neutral hydrogen atom (H_I) provides a unique means of mapping large-scale structures (LSS) over a wide range of redshifts in the post-reionization era ($z < 6$) [1, 2]. The collective 21-cm emission from individual H_I sources in the post-reionization era creates a diffuse background radiation below 1420 MHz. Detecting intensity fluctuations in this 21-cm background can offer insights into the underlying LSS, a technique known as 21-cm intensity mapping [3–5]. This method allows the surveying of extensive cosmic volumes using current and upcoming radio telescopes [4, 6, 7].

In order to analyze the 21-cm intensity fluctuations, one of the choices is to compute the power spectrum of the intensity field. In the post-reionization era, the lack of complex

reionization astrophysical processes in the intergalactic medium (IGM) makes the 21-cm power spectrum directly related to the underlying matter power spectrum [8] as well as underlying cosmology. Detecting Baryon Acoustic Oscillations (BAO) in the 21-cm power spectrum can provide precise constraints on the expansion rate of the universe, or on the equation of state for dark energy [9–12]. Accurate measurement of the 21-cm power spectrum also holds promise for independently estimating various cosmological parameters [7, 13, 14]. Cross-correlating the 21-cm signal with other tracers of LSS, such as the Lyman α forest [15–17], Lyman-break galaxies [18], weak lensing [19], and the integrated Sachs-Wolfe effect [20], has been proposed as essential cosmological probes in the post-reionization era.

Several low-frequency instruments, including BINGO [21, 22]¹, CHIME [23]², Tianlai Project [24]³, FAST [25]⁴, ASKAP [26]⁵, HIRAX [27]⁶, CHORD [28]⁷, SKA [29]⁸ are planned to measure the 21-cm signal at various redshifts of the post-reionization era. Recently, [30] has reported the possible first detection of the 21-cm autocorrelation power spectrum at $z \sim 0.32$ and 0.44 using the MeerKAT radio telescope. So it is expected that the signal will be detected at even higher redshifts in the post-reionization era.

The 21-cm signal is inherently weak, several orders of magnitude smaller than various astrophysical foregrounds [31–33]. The observed data from the present generation telescopes is mostly foreground and systematics dominated and we are yet to find an optimal method to isolate the signal from the contaminations. However, once this hurdle is over, we expect to detect the post-reionization 21-cm signal. We therefore need accurate models of the 21-cm signal to be able to estimate the amplitude and features of the power spectrum expected from observations. Not only that, we need accurate modelling to interpret the signal as well [34, 35].

Significant efforts have been devoted to modelling the post-reionization H I distribution and the expected 21-cm signal. A number of analytic [36–38], semi-numerical [39–46], and fully numerical techniques [47–51] have been implemented to simulate the H I distribution and model the 21-cm signal statistics across the post-reionization redshifts. In this work, we rely on a semi-numerical simulation technique where the dark matter halos identified from N-body simulations are populated with H I using an analytic prescription. For a comprehensive review of this technique, the reader is referred to the following references [39–42, 45].

The standard cosmological model suggests that the initial density perturbations were largely Gaussian in nature [52]. As the density fields evolve, non-Gaussianity is introduced due to the non-linearity in the fields induced by the flow of matter towards the high-density peaks at the biased locations in the Universe [53]. Also, a number of studies suggest that there may be a primordial non-Gaussianity component in the density fields [54]. Therefore, we need to consider primordial non-Gaussianity along with the induced non-Gaussianity in order to probe the complete information in the field. Whatever the scenario, ultimately,

¹<https://bingotelescope.org/>

²<https://chime-experiment.ca/en>

³<https://tianlai.bao.ac.cn/>

⁴<https://fast.bao.ac.cn>

⁵<https://www.atnf.csiro.au/projects/askap/index.html>

⁶<https://hirax.ukzn.ac.za>

⁷<https://www.chord-observatory.ca>

⁸<https://www.skatelescope.org/>

we have non-Gaussian matter distribution in the post-reionization era [55–62]. The post-reionization 21-cm signal is expected to be non-Gaussian in nature as it directly follows the non-Gaussian matter distribution [63]. Note that, unlike in the reionization 21-cm signal where the non-Gaussianity is majorly induced by the inhomogeneities in the radiation, heating, and ionization of the IGM gas, [64, 65] the non-Gaussianity in the post-reionization 21-cm signal is dominated by the density fields.

The two-point correlation or its Fourier conjugate, the power spectrum, is not an exhaustive statistic to capture the time-evolving non-Gaussianity in a field. For a Gaussian field, the power spectrum is sufficient to describe the field. However, for non-Gaussian fields, like the 21-cm signal, we need to think about ways to pick up information beyond the two-point correlation. One of the ways is to estimate higher-order correlations like the three- and four-point functions, or their Fourier conjugate, namely, bispectrum [63], and trispectrum [66]. Calculating higher-order functions can be computationally expensive, although recent advancements show a significant speed-up in the computation [58, 67, 68]. Further, higher-order statistics can be difficult to interpret. Alternative ways include different summary statistics [69, 70], strategies to segment the density field and calculate correlation, constructing marked fields, and studying their statistics that may contain the information of some higher-order moments [71–74]. For our current study, we mostly focus on the last alternative.

Several studies suggest and we shall also show in this work, the amplitude and shape of the H I density power spectrum (Δ_{HI}^2) at small k ($< 1 \text{ Mpc}^{-1}$) do not evolve significantly across $1 < z < 5$ [39–44, 46, 49]. On the other hand, the matter clustering grows significantly in this same z range. Not only that, the H I content of the dark matter halos, the H I mass function, and the cosmological H I (although, observationally, this has been found to change marginally over z , e.g. see [75]), all evolve with z . The power spectrum mostly captures information from high-density regions. Therefore, it is expected to be sub-optimal for extracting information embedded in low-density regions and we shall not get any information on the H I evolution at all densities by studying only Δ_{HI}^2 .

In this work, we explore whether the marked power spectrum of the H I density field can characterize clustering patterns in H I distribution at different length scales. A mark of a field is a transformation of that field around each point. Mark usually depends on the properties of the considered field. Marked power spectrum is the Fourier conjugate of the two-point correlation function of the marked field. Since, in general, a mark is a non-linear function of the original field, the two-point marked correlation function not only contains the information of the original two-point correlation function but also at least some of the next higher-order correlation functions of the field. Here we study how the marks on the H I density fields enable us to study the evolution and properties of the H I distribution at various scales. The application of marked statistics to the 21-cm signal here is the first of its kind for studying the post-reionization Universe. The marked power spectrum, however, has previously been used, for example, to detect the neutrino mass in the dark matter density distribution [76] and information in the galaxy distribution [77]. Estimating the marked power spectrum in this work is easy because all that it requires is a functional form of the local density as the mark. We just need to add this mark to the pipeline that computes the power spectrum while correlating the two marked points in order to estimate the marked power spectrum.

Several previous studies have shown that certain non-linear transformations Gaussianize the density field up to an extent [78, 79]. These transformations, therefore, turn the information inherent in the higher-order functions back to what we expect to obtain from the two-point correlations. This, thus, provides us with a way to improve the parameter constraints that are likely to be obtained from the two-point correlations.

The paper is organized as follows. In section 2 we present the HI simulation. Section 3 describes the formalism of the marked correlation function and the marked power spectrum. In section 4 we discuss our analysis of the marked power spectra. Section 5 presents a summary and discussion.

Throughout this paper, we have adopted the Planck+WP best-fit cosmological parameters $h = 0.6704$, $\Omega_m = 0.3183$, $\Omega_\Lambda = 0.6817$, $\Omega_b h^2 = 0.022032$, $\sigma_8 = 0.8347$, $n_s = 0.9619$ from ref. [80].

2 Simulating the HI distribution in the post-reionization era

We simulate the HI distribution in the post-reionization era following three major steps.

2.1 *N*-body simulation

First, we simulate the dark matter distribution and velocity at redshifts in the range $z \in [1, 5]$ in steps of $\Delta z = 1$, using a publicly available ‘dark-matter only’ particle mesh (PM) *N*-body code⁹ [81]. The simulations start with $[1072]^3$ dark matter (DM) particles, each having a mass $1.09 \times 10^8 M_\odot$, on $[2144]^3$ regular grids with a spatial resolution of 70 kpc. This sets the comoving volume of our simulations to be $[150.08 \text{ Mpc}]^3$. The initial conditions are set at $z = 125$ using the linear Λ CDM power spectrum [82] and the Zel’dovich approximation [83]. Starting from this, the *N*-body code then evolves the particle positions and velocities to desired redshifts in the range $z \in [1, 5]$ and generates comoving dark matter snapshots.

2.2 Finding FoF halos

Next, we identify the collapsed dark-matter halos in the DM distribution by using a publicly available halo finder code¹⁰ that employs the Friends-of-Friend (FoF) algorithm [84]. Here, we set the linking length to 0.2 in units of mean inter-particle spacing. We further impose a condition that a cluster of particles must at least have 10 members to be identified as a halo, which sets the halo mass resolution to $M_{h,\min} = 1.09 \times 10^9 M_\odot$ in our simulations. The mass distribution of these FoF halos is also verified to be in good agreement with the theoretical halo mass function [85, 86] in the range $10^9 \leq M_h \leq 10^{13} M_\odot$.

2.3 Simulating HI using $M_h - M_{\text{HI}}$ relation

Finally, we populate the identified FoF halos with HI. We use an analytic prescription for populating the halos. Ref. [39] have proposed several schemes to connect HI mass to the

⁹<https://github.com/rajeshmondal18/N-body>

¹⁰<https://github.com/rajeshmondal18/FoF-Halo-finder>

z	f_3	$M_{\text{h,min}}$ ($10^9 M_\odot$)	$M_{\text{h,max}}$ ($10^{11} M_\odot$)
1	0.016	3.53	10.47
2	0.017	1.92	5.70
3	0.020	1.25	3.70
4	0.025	0.89	2.65
5	0.035	0.68	2.02

Table 1. List of the values of the free parameter f_3 in $M_{\text{h}} - M_{\text{HI}}$ relation 2.1, $M_{\text{h,min}}$ and $M_{\text{h,max}}$ calculated using Equation 2.2 at different redshifts.

halo mass in the post-reionization era. In our work, we have considered the third scheme which connects HI mass to halo mass as:

$$M_{\text{HI}}(M_{\text{h}}) = \begin{cases} f_3 \frac{M_{\text{h}}}{1 + \frac{M_{\text{h}}}{M_{\text{h,max}}}}, & \text{if } M_{\text{h}} \geq M_{\text{h,min}} \\ 0, & \text{otherwise.} \end{cases} \quad (2.1)$$

$M_{\text{h,min}}$ and $M_{\text{h,max}}$ in this equation can be calculated using an approximate relation that connects the halo mass with the virial circular velocity (v_{circ}) of the halo as:

$$M_{\text{h}} \simeq 10^{10} M_\odot \left(\frac{v_{\text{circ}}}{60 \text{ km s}^{-1}} \right)^3 \left(\frac{1+z}{4} \right)^{-\frac{3}{2}}. \quad (2.2)$$

The $M_{\text{h}} - M_{\text{HI}}$ relation 2.1 assumes that the HI inside a halo survives only when the halo circular velocity exceeds a value of $\sim 30 \text{ km s}^{-1}$, which determines the minimum threshold $M_{\text{h,min}}$. The upper limit $M_{\text{h,max}}$ is set by plugging $v_{\text{circ}} \sim 200 \text{ km s}^{-1}$, above which the HI fraction in halos seems to decrease as suggested by simulations. The values of $M_{\text{h,min}}$ and $M_{\text{h,max}}$ at different z are tabulated in Table 1. Note that, at $z = 3.5$, $M_{\text{h,min}} = 10^9 M_\odot$ which is also the minimum mass of halos that we can resolve in our simulations. At $z > 3.5$, HI is allowed to reside inside halos with mass smaller than $M_{\text{h}} < 10^9 M_\odot$ which we cannot resolve given the mass resolution of our current setup. However, ref. [42] discussed that ignoring the smaller halos has a very minor effect on the HI power spectrum even at $z \sim 6$.

This scheme is based on the following arguments. The majority of HI in the post-reionization era is seen to be confined to dense clouds, known as Damped Lyman Alpha systems (DLAs), with column densities of $N_{\text{HI}} \geq 2 \times 10^{20} \text{ cm}^{-2}$. These DLAs are observed in the absorption spectra of distant quasars (QSOs) [87], which also shows that very little HI is left in the intergalactic medium at $z < 5$. DLAs are hosted by galaxies that form inside the dark matter halos. Therefore, it is safe to assume that the total HI in the post-reionization universe is locked inside the halos. We also assume that the HI content of a halo solely depends on the halo mass M_{h} , and within each halo HI is distributed uniformly, rather than being contained within the substructures, like galaxies. A halo, however, needs to be above some critical threshold mass $M_{\text{h,min}}$ to be able to self-shield the HI content against the harsh ionizing UV background [88–90]. The HI content of a halo above this threshold typically

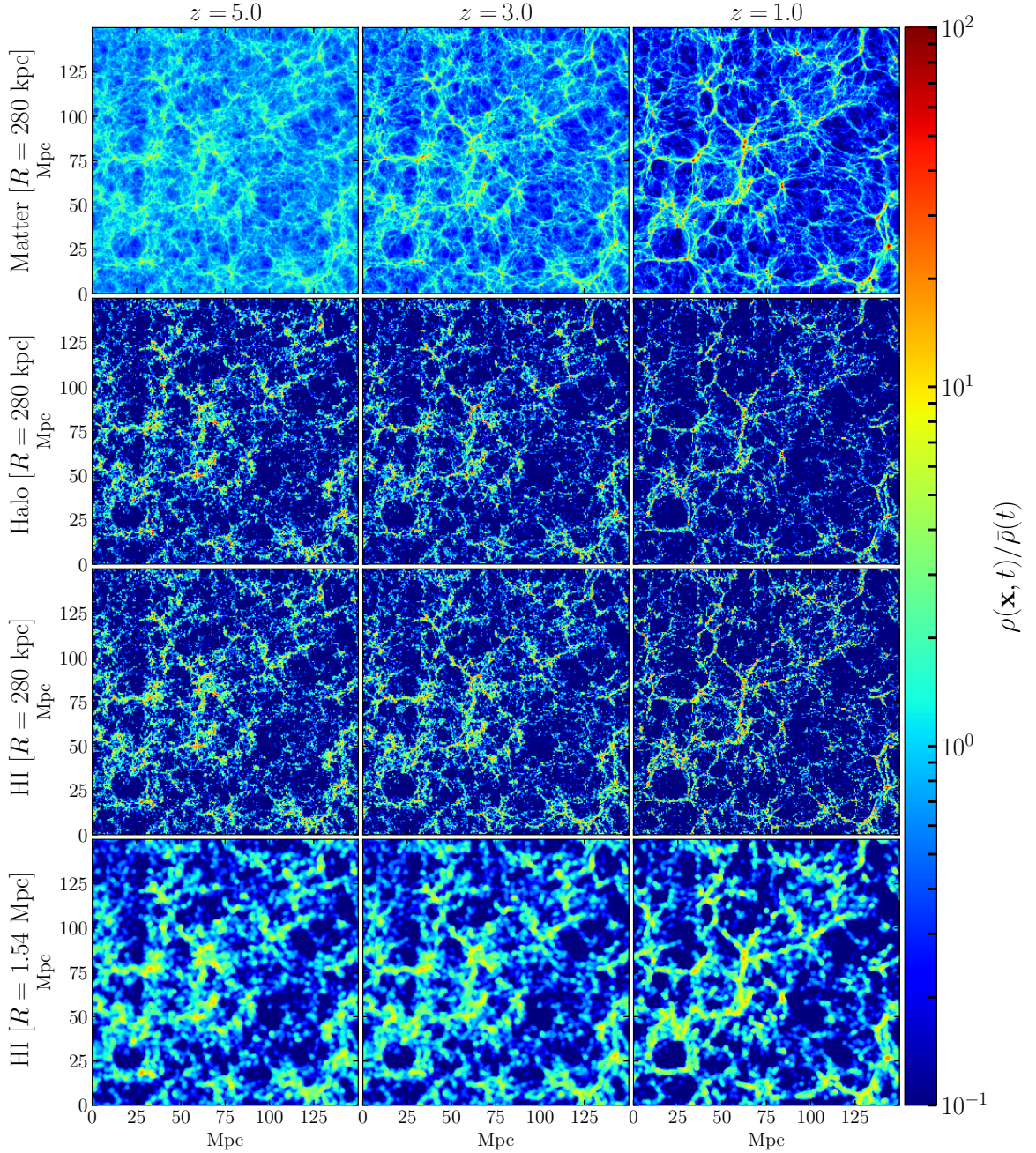


Figure 1. Visuals of matter (top first row), halo (second row) and HI (third row) density distributions shown at three different redshifts $z = 5, 3,$ and $1,$ showing high-resolution distributions obtained after smoothing of this field using a spherical top hat filter for a fixed radius of $R = 280$ kpc (grid cell size). Panels in the bottom row show the low-resolution HI density distribution which is smoothed for $R = 1.54$ Mpc. For this, we first compute the densities on the grid points using the cloud-in-cell (CIC) interpolation scheme. We then plot the 2D slices showing the mean density on a plane after compressing a layer of thickness 5.6 Mpc along a direction.

increases with the halo mass. Several low-redshift observations indicate that the HI content drops for massive halos, typically above some threshold mass $M_{h,\max}$ [91, 92]. Therefore, it is expected that the halos having mass in the range $M_{h,\min} \leq M_h \leq M_{h,\max}$ contain most of the HI.

Scheme 2.1 allows the halos with mass above $M_{h,\min}$ to host HI. The HI mass (M_{HI}) inside a halo increases with the halo mass linearly until the halo mass attains a value $M_{h,\max}$ at which M_{HI} saturates to a value $M_{\text{HI}} \approx (f_3)M_{h,\max}$. Therefore, for halos with $M_h > M_{h,\max}$, the M_{HI} remains almost constant. The free parameter f_3 is adjusted by requiring that the cosmological HI density parameter $\Omega_{\text{HI}}(z)$ from simulations matches the observations [93–95]. The values of f_3 at different redshifts are listed in Table 1.

We have run our simulations for five statistically independent realizations. We use these realizations to estimate the mean and the standard deviation for all the results shown in this article. In Figure 1, we plot visualization of the density field $\rho(\mathbf{x}, z)/\bar{\rho}(z)$, the ratio of the density at \mathbf{x} over the mean density, for matter (top first row), halo (second row), and the HI (third and fourth row) for a single realization and at three different stages of cosmic evolution, $z = (5, 3, 1)$. The color bar in the log scale shows a clear evolution of the densities in the large range of their distributions. The matter and halo densities are smoothed using a spherical top hat filter of a fixed comoving radius of $R = 280$ kpc, while the HI density is shown at two different resolutions obtained after smoothing of the distribution at comoving radii $R = 280$ kpc and 1.54 Mpc. Here, $R = 280$ kpc is the, minimum possible scale (grid cell size) of smoothing in our simulation, whereas $R = 1.54$ Mpc represents the typical resolution of the intensity mapping experiments.

A number of studies have shown that the scatter in the galaxy and halo luminosities impact the galaxy line intensity mapping signal and its statistics significantly over a wide z -range [96–98]. This scatter is also expected to impact the HI distribution in the post-reionization era. We have not considered the effect of scatter in this paper.

3 Formalism of marked statistics

3.1 The marked correlation function

Two point marked correlation function (MCF) in configuration space is defined as [99, 100]

$$\mathcal{M}(x) = \frac{1}{n(x)\bar{m}^2} \sum_{ij} m_i m_j = \frac{1 + W}{1 + \xi}, \quad (3.1)$$

where $n(x)$ is the number of pairs at separation x in a field, the summation over which is needed to get the value of \mathcal{M} . m_i is the mark at i_{th} point with a mean \bar{m} over the entire sample. The second equality is set to define W which is normalized by the two-point correlation function (ξ) to emphasize the \mathcal{M} to be 1 at large scales. \mathcal{M} is easy to compute if one already has a pipeline to compute the standard two-point correlation function. It only requires a simple modification to the correlation function calculations.

The correlations of the marked point processes for the first time were introduced by [101]. A wide range of astrophysical and cosmological applications of the MCF have subsequently been made. This, for example, has been used to study how the bars and bulges

in disc galaxies depend on the environment [102]. This also offers a way of testing the connection between galaxy clustering and galaxy properties such as luminosity, morphology, color, star formation rate, stellar mass, etc. [99, 103–105]. Furthermore, the marked statistics are able to trace the alignment of dark matter halos in the distribution of the dark-matter particles [104], and to probe the dependence of clustering of these halos on merger history [106]. A halo model description of the MCF was developed in [107]. The MCF has also been used to break degeneracies in different halo occupation distribution (HOD) models [108]. In the past decade, marked statistics have extensively been used to demonstrate how different modified gravity (MG) models are distinguished from general relativity (GR), due to the strong dependence of the tracer on the environment in MG models [100, 109–117].

3.2 The choices of the mark

In this work, we use the mark as a function of local density (ρ_R) formulated by [100], and given as

$$m(\mathbf{x}, t; R, \rho_*, p) = \left[\frac{\rho_* + 1}{\rho_* + \rho_R(\mathbf{x}, t)} \right]^p, \quad (3.2)$$

where, the free parameters R , ρ_* , and p are known as the mark parameters. Here, both ρ_R and ρ_* are in unit of mean density $\bar{\rho}$. The parameter ρ_* reveals how strongly the mark is sensitive to the local density around each point. The exponent p introduces an additional contrast between two points in different environments by weighting these points differently. Note that the choice of the functional form of the mark, as well as the values of the free parameters, is arbitrary, but needs to be chosen according to the properties of the given field and the information that we are interested in extracting from that field.

The idea of using the mark as a function of local density was first proposed by [108] to constrain HOD models in order to study which galaxies reside inside which halos. The mark m was introduced to deal with cases where we have a smoothed field of the observable. m was designed as a function of ρ_R , smoothed over some radius R using filters like spherical top-hat, for extracting the information around the objects without knowing their own properties. The observations of the redshifted 21-cm signal using the intensity mapping techniques are expected to produce low-resolution maps of the 21-cm intensity fluctuations. Since the H I density field is proportional to the 21-cm intensities, we therefore can use the H I density to define the mark as given by equation 3.2. We apply this mark at all the H I redshift snapshots and create marked H I fields for studying the H I clustering and evolution with time in the post-reionization era. We have also considered a different functional form for the mark proposed in [108] and defined in equation A.1. We found that this mark is not very useful for our purpose and we briefly discuss the associated results in Section A.1. From here onwards, we shall focus mainly on the mark defined in equation 3.2.

For $\rho_* \rightarrow 0$, the mark m is informative as it scales as $m \approx [1/\rho_R]^p$. This suggests that, for positive p (which we designate as $p_{\text{ld}1}, p_{\text{ld}2}, \dots$ for $p = 1, 2, \dots$), m gives more weight to underdensities and therefore is sensitive to the information in the underdense regions. On the other hand, for negative p (which we refer to as p_{hd} for $p = -2.0$, as we have considered only one negative value), m applies more weight to overdensities and probes features from the overdense regions. Table 2 lists the values of free parameters used in this paper.

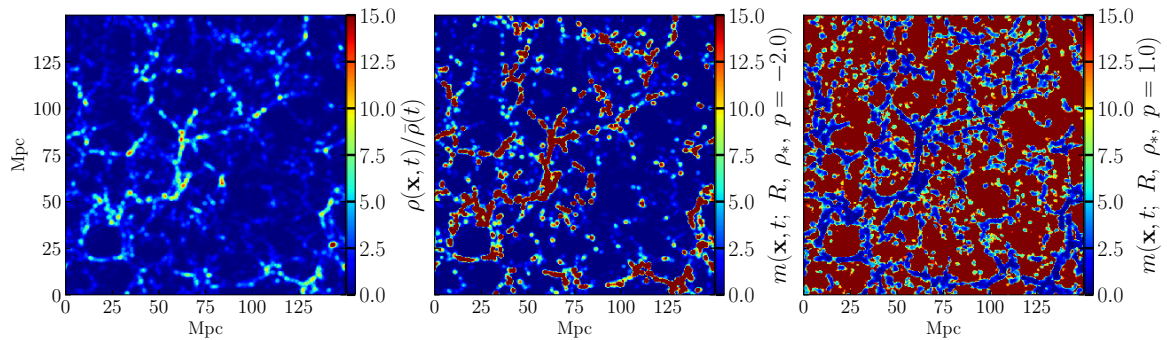


Figure 2. **Left panel:** H I density field at redshift $z = 1$ which is smoothed for a radius $R = 1.54$ Mpc. **Middle and Right panels:** Marked H I density fields at $z = 1$, with parameters $R = 1.54$ Mpc, $\rho_* = 0.01$ and for p_{hd} (middle panel) and p_{ld1} (right panel).

$\rho_*/\bar{\rho}$	p	R (Mpc)
0.01	-2.0 (p_{hd})	0.28 1.54
0.01	1.0 (p_{ld1})	0.28 1.54
0.01	2.0 (p_{ld2})	0.28 1.54

Table 2. List of the values of the free parameters of the mark m (eq. 3.2) considered in this paper. We designate positive p as p_{ld1} , p_{ld2} for $p = 1, 2$. On the other hand, we designate negative p as p_{hd} for $p = -2.0$, as we have considered only one negative value.

Figure 2 shows a visual comparison between the standard H I density field (left panel) together with the two marked density fields (middle panel for p_{hd} and right panel for p_{ld1}). Comparing the left and middle panels, we see that the high-density regions in the middle panel are very prominent as compared to the left panel which is exactly what we expect for the mark with p_{hd} . On the other hand, doing the same comparison between the left and right panels, we find that the underdense regions are enhanced in the right panel for p_{ld1} . Since for the standard density field, the power spectrum mostly picks contributions from the high-density regions, we expect the marked power spectrum for p_{hd} to exhibit similar features as in the power spectrum for the standard density field. On the other hand, the marked power spectrum with p_{ld1} is expected to show different behaviour and contain additional information as compared to the standard density power spectrum.

4 Results

Figure 1 shows the features that we can visually infer by looking at the dark matter, halo, and H I density snapshots. The halo field closely follows the dark matter density peaks. Also, the

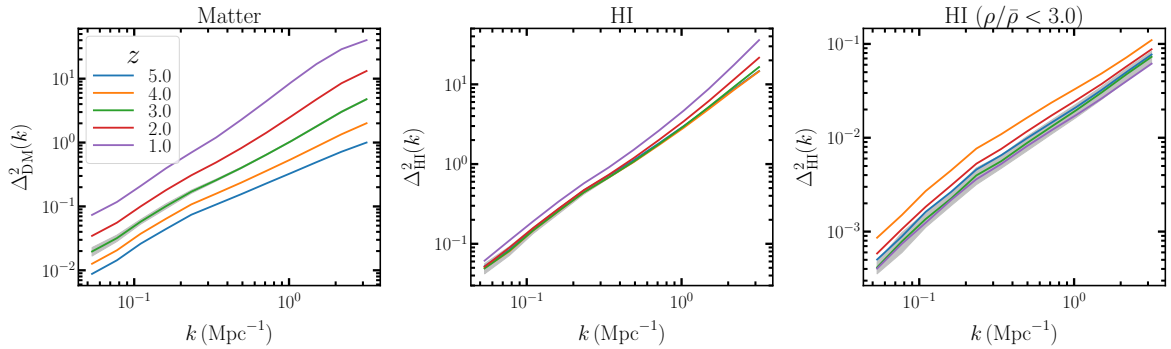


Figure 3. The dimensionless power spectrum of the matter (left panel), the HI (middle panel), and the HI with density values $[\rho/\bar{\rho}] < 3.0$ (right panel). The distribution is smoothed for a fixed radius of $R = 280$ kpc. The power spectra are demonstrated as a function of k -mode at five different redshifts in the range $z \sim 1$ –5. The shaded regions in each panel represent $\pm 1\sigma$ spread around the mean value at $z = 3$.

HI distribution traces the halo distribution at all z , which is expected as we have populated the halos with HI. The dark matter clustering grows with time, as we go to lower z . As a result, the halos grow in mass and number with decreasing z , which results in the growth of the density contrast. According to the HI population model in Equation 2.1, the HI mass inside the halos exceeding a certain cut-off mass $M_{h,\max}$ remains almost fixed. As a result, although the halos grow in mass with time and the halo density contrast increases, halos that surpass the upper threshold do not show any enhancement in density contrast for HI. On the other hand, some halos that were devoid of any HI at higher redshifts and cross the minimum threshold $M_{h,\min}$ at any lower z , appear as new overdense regions in HI distribution and contribute to the evolution of the HI field. However, it is difficult to locate these changes visually from Figure 1. Thus, the HI distribution is biased against the dark matter distribution. Visually, the HI distribution, on the contrary of matter and halo distribution, evolves only weakly with z due to this HI density bias.

In Figure 3, we show the evolution of the spherically averaged dark-matter power spectrum ($\Delta_{\text{DM}}^2(k)$ in the left panel), along with the HI density power spectrum ($\Delta_{\text{HI}}^2(k)$ in the middle panel) in the redshift range $z \in [1, 5]$. In order to understand the weak evolution of $\Delta_{\text{HI}}^2(k)$ with z , in the right panel, we have plotted the HI power spectrum for low- and intermediate-density regions where $[\rho/\bar{\rho}] < 3$ (which we refer to as $\Delta_{\text{HI(LID)}}^2(k)$). Here, we have normalized the power spectrum to the dimensionless quantity $\Delta^2(k) = k^3 P(k)/2\pi^2$. We use five realizations of the simulations, each providing a statistically independent estimate of the power spectrum, to compute the mean and standard deviations. The lines in the figures show the mean at different redshifts and a shaded region around the mean shows $\pm 1\sigma$ standard deviation. Note that the power spectrum and marked power spectrum have been estimated using a grid 4 times coarser than the one we used for the N -body simulations. In the following sections, we also restrict our analysis to k modes in the range $0.05 \lesssim k \lesssim 1.0$ Mpc^{-1} and smoothing radii in the range $0.28 \lesssim R \lesssim 5.0$ Mpc .

Considering the left panel of Figure 3, we find that $\Delta_{\text{DM}}^2(k)$, starting from $z = 5$, grows

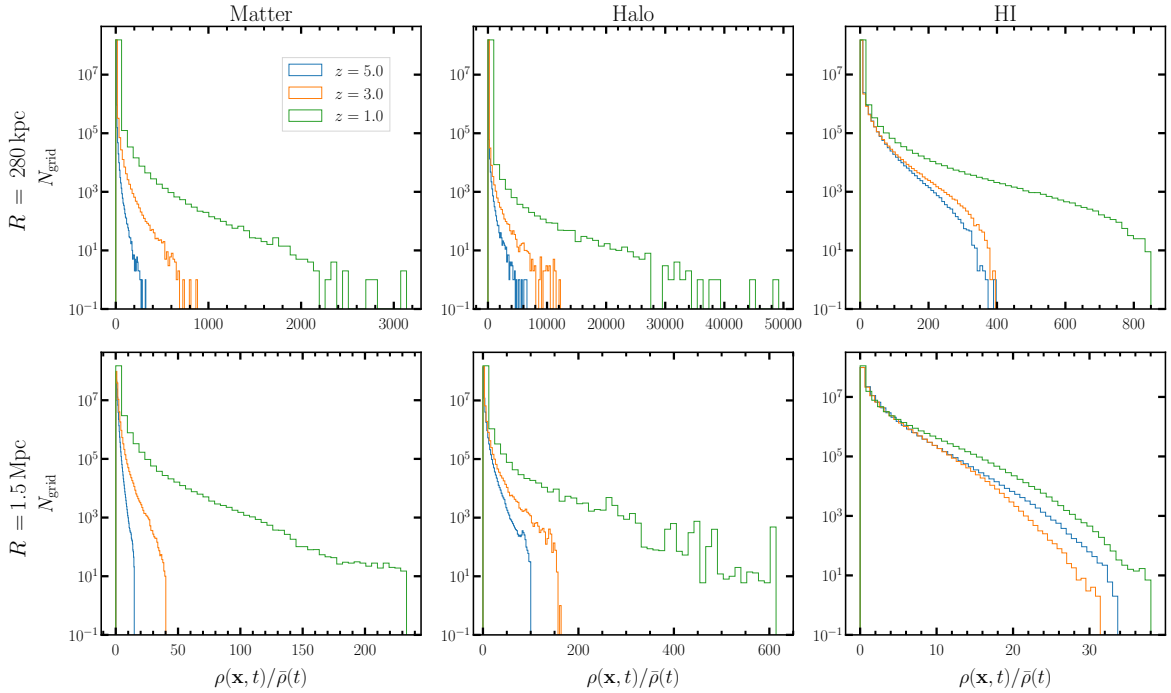


Figure 4. Histogram of the density distributions of the matter (left column), halo (middle column), and HI (right column) on the grids in the simulation volume at three different redshifts, $z = (1, 3, 5)$. The upper and lower panels are shown respectively for two different R values; $R = 280$ kpc and 1.54 Mpc. The different histograms in each panel show how the density is being evolved over the cosmic time in the post-reionization era.

considerably with decreasing z . This is due to the growth in dark matter clustering with time owing to gravitational instability. At $k < 1 \text{ Mpc}^{-1}$, $\Delta_{\text{DM}}^2(k)$ shows nearly a power law behaviour with k . Considering the middle panel, we find that $\Delta_{\text{HI}}^2(k)$ also shows a similar power law behaviour with k . However, contrary to $\Delta_{\text{DM}}^2(k)$, $\Delta_{\text{HI}}^2(k)$ shows very little evolution over z . In the right panel, we see that $\Delta_{\text{HI(LID)}}^2(k)$ exhibits considerable variations with z indicating that the clustering at low and intermediate densities evolves with z . However, comparing the right and the middle panels, we see that the amplitude of $\Delta_{\text{HI(LID)}}^2(k)$ is nearly two orders of magnitude smaller than that of the total HI power spectrum. Therefore, even though these regions evolve, their overall contribution is negligible in comparison to the high-density regions. We have already discussed in the context of Figure 1 that the high-density HI regions do not show considerable enhancement in clustering with z due to the HI density bias. This is the main reason for the weak redshift evolution of $\Delta_{\text{HI}}^2(k)$ over time in the middle panel. Even though there is a significant evolution in the low-density HI regions, the same is not captured well by the power spectrum.

In order to understand the evolution of HI densities relative to the densities of matter and halos, we show the histogram of the quantity $\rho(\mathbf{x})/\bar{\rho}$ for the three fields at three redshifts in Figure 4. Note again that these densities are computed on the grids. We have used two different smoothing radii $R = 280$ kpc and $R = 1.54$ Mpc for computing the densities.

Considering all the panels, we see that the evolution of the histogram with z is weaker for HI compared to both matter and halos. This weaker evolution in HI is substantial to consider for studying the HI clustering using the intensity mapping experiment. This conclusion remains the same for the two different aforementioned smoothing scales.

The evolution of the HI field can be visualized alternatively by plotting the quantity $\Delta(\rho/\bar{\rho})(\mathbf{x}, z) = (\rho/\bar{\rho})(\mathbf{x}, z) - (\rho/\bar{\rho})(\mathbf{x}, z = 5)$, where $(\rho/\bar{\rho})(\mathbf{x}, z)$ is defined at (\mathbf{x}, z) and $(\rho/\bar{\rho})(\mathbf{x}, z = 5)$ is the same field but defined at $z = 5$. The top two rows of Figure 6 show this quantity at three redshifts $z = 4, 3$ and 1 and for two different R . $\Delta(\rho/\bar{\rho})$ here captures the change in the HI density at a point due to gravitational clustering relative to $z = 5$. In other words, $\Delta(\rho/\bar{\rho})$ captures the transfer of HI from low-density regions to high-density regions due to the growth of structures. We see that for each R , $\Delta(\rho/\bar{\rho})$ changes considerably with z . $\Delta(\rho/\bar{\rho})$ is low at higher z and high at lower z due to the evolution of HI with time. Also, this change depends on R , which is larger for $R = 280$ kpc compared to that for $R = 1.54$ Mpc. Thus, the HI density shows evolution, and this evolution is not captured well enough by the normal power spectrum.

Before applying the mark, it is essential to decide on the values of the mark parameters, R , ρ_* , and p , as the various combinations of these determine the different features that can be extracted from the density fields. We consider a total of six combinations of the mark parameters listed in Table 2. In general, the parameter R can take any arbitrary value, but in practice, it should be chosen to match the resolution of a particular experiment. The choice of parameter ρ_* is also very crucial as this is added to the density at each grid, shifting the mean value of the field. Further, in practice, there may be inherent noise in the density field estimation and, therefore, we choose smaller p values, $|p| \leq 2.0$, to prevent the noise from getting amplified. We recapitulate once more that with p_{ld1} or p_{ld2} , the mark m gives more weight to the underdensities. Whereas, p_{hd} applies more weight to the overdensities.

4.1 The Fourier mode (k) dependence of the marked HI power spectra (MPS)

In Figure 5, we show the marked fields for p_{hd} and p_{ld1} , at three redshifts and for two R values, 280 kpc and 1.54 Mpc. Note that unless otherwise stated, ρ_* is kept fixed at 0.01 for all the figures. The impact of considering different values of ρ_* on the results has also been discussed in the section A.2. Keeping Figures 1 and 5 side by side, we can broadly say that the over-dense regions in Figure 1 (last two rows) are enhanced for p_{hd} and are suppressed for p_{ld1} . For example, the prominent overdensity at box location $\sim (75, 75)$ Mpc is enhanced for p_{hd} and is suppressed for p_{ld1} . Further, the mark with p_{ld2} only enhances the contrast between high and low-density regions, giving more weight to the overdensities.

4.1.1 MPS for p_{hd}

In order to visualize the evolution found in Figure 5 in an alternative way, we have plotted the quantity $\Delta m(\mathbf{x}, z) = m(\mathbf{x}, z) - m(\mathbf{x}, z = 5)$ in Figure 6 at three redshifts. The middle and the last two rows in this figure respectively show Δm with p_{hd} and p_{ld1} , calculated using two R values. Considering the two middle rows, we find that the basic web structure is similar to that of the top two rows which represent $\rho/\bar{\rho}$, only the amplitude of the overdensities increased. Also, the redshift evolution of the high-density peaks looks more prominent than in $\rho/\bar{\rho}$.

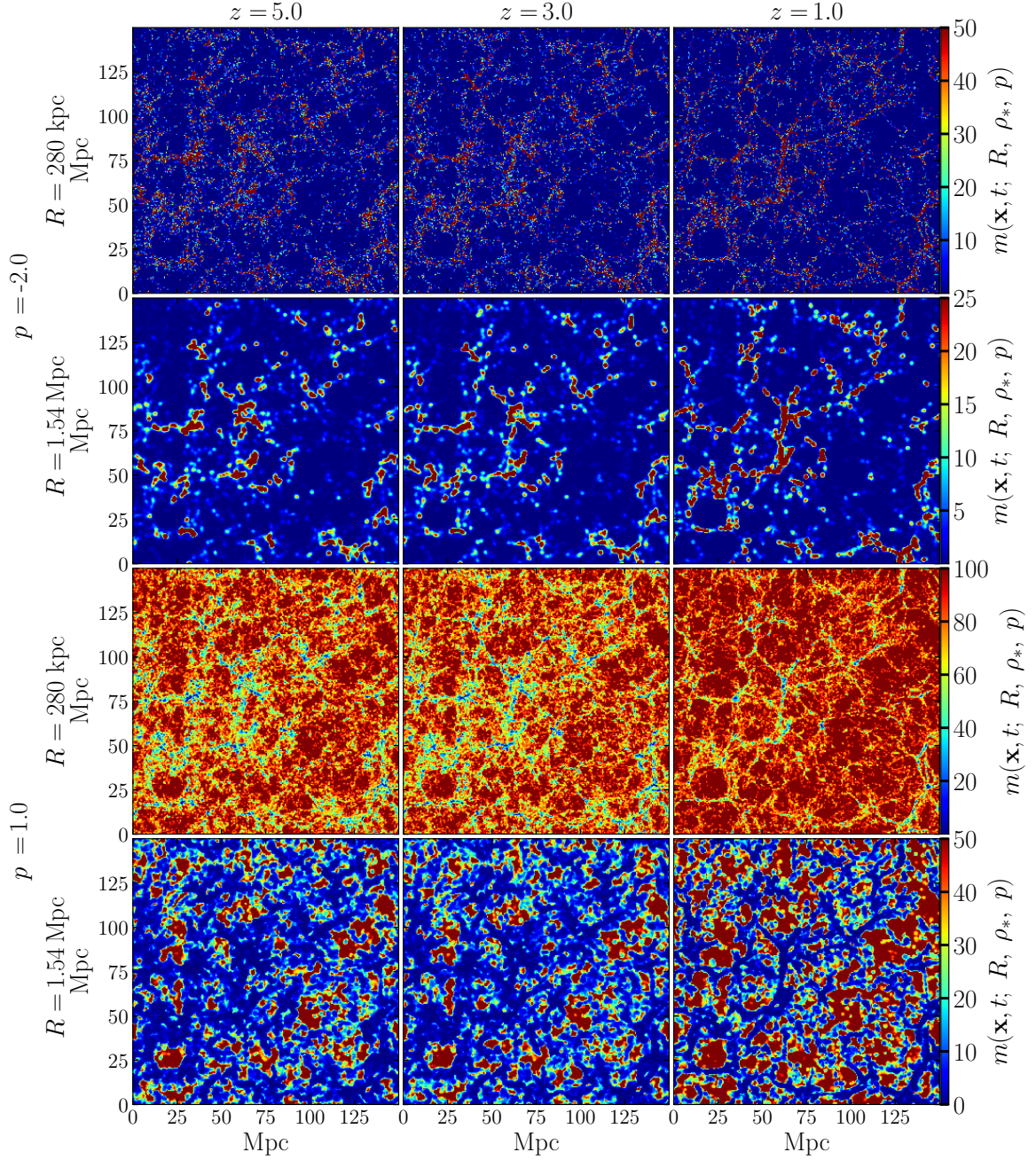


Figure 5. Marked Hi field (m) at different redshifts (decreasing from left to right) and for different mark parameters (varying in the vertical direction). Here, the value of the parameter ρ_* is 0.01. The top two rows show the time evolution in m for two different radii $R = 280 \text{ kpc}$ and $R = 1.54 \text{ Mpc}$ and for a fixed parameter p_{hd} . The bottom two rows show the same but now for p_{ld1} .

We shall now use the MPS to statistically verify whether this intuition is correct. In Figure 7, we show the MPS (Δ_m^2) at various redshifts for different values of the mark parameters p and R . Considering the left column, which shows Δ_m^2 for p_{hd} with two R values

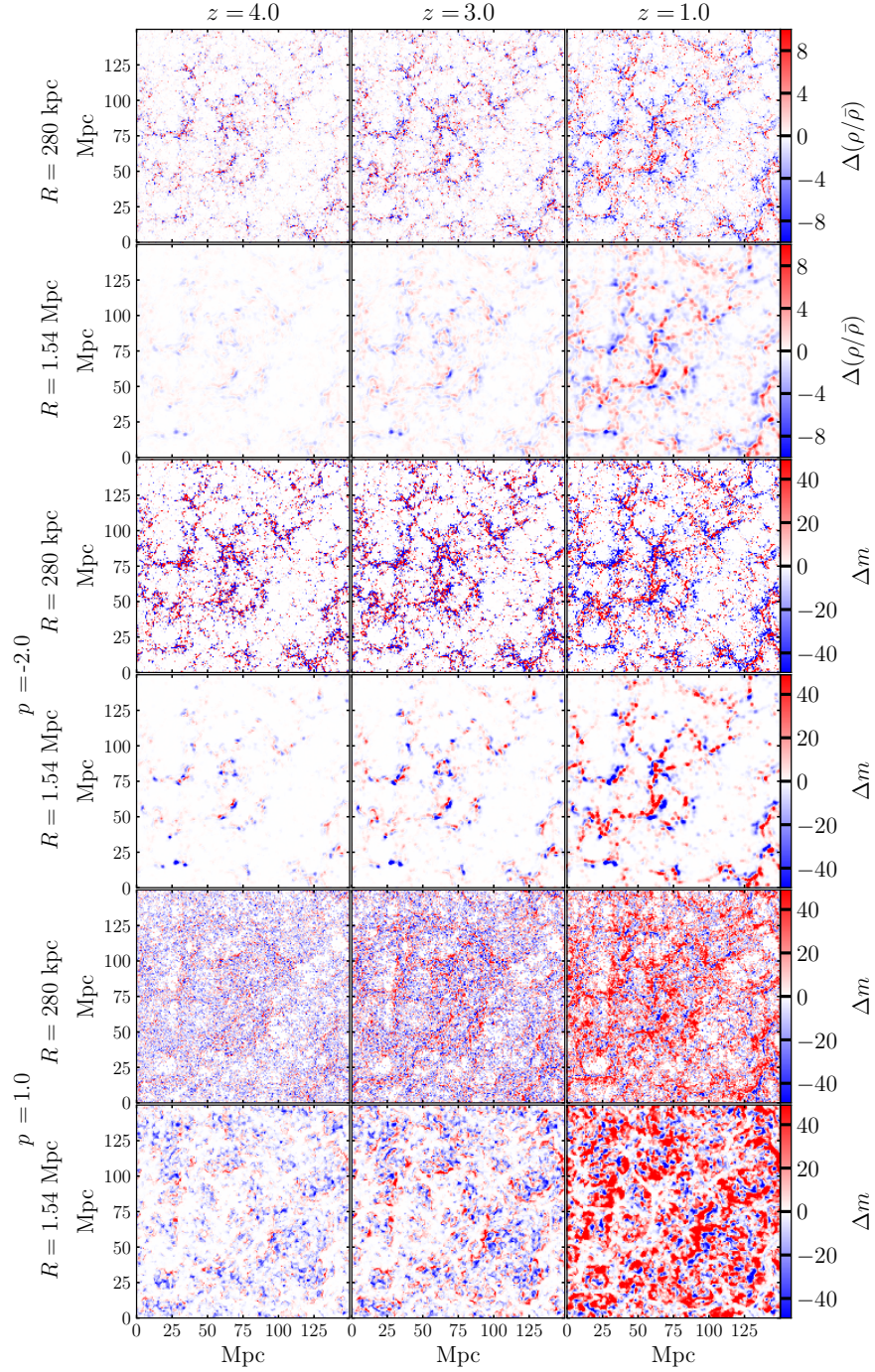


Figure 6. **Top two rows:** The quantity $\Delta(\rho/\bar{\rho})(\mathbf{x}, z) = (\rho/\bar{\rho})(\mathbf{x}, z) - (\rho/\bar{\rho})(\mathbf{x}, z = 5)$ and **bottom four rows:** $\Delta m(\mathbf{x}, z) = m(\mathbf{x}, z) - m(\mathbf{x}, z = 5)$ that alternatively visualizes the evolution found in Figure 5. For a particular field, this represents the difference in the field at any z and $z = 5$ for two R values i.e., $R = 280$ kpc and 1.54 Mpc. The two middle and two bottom rows respectively show the difference for the marked field m with p_{hd} and p_{ld1} .

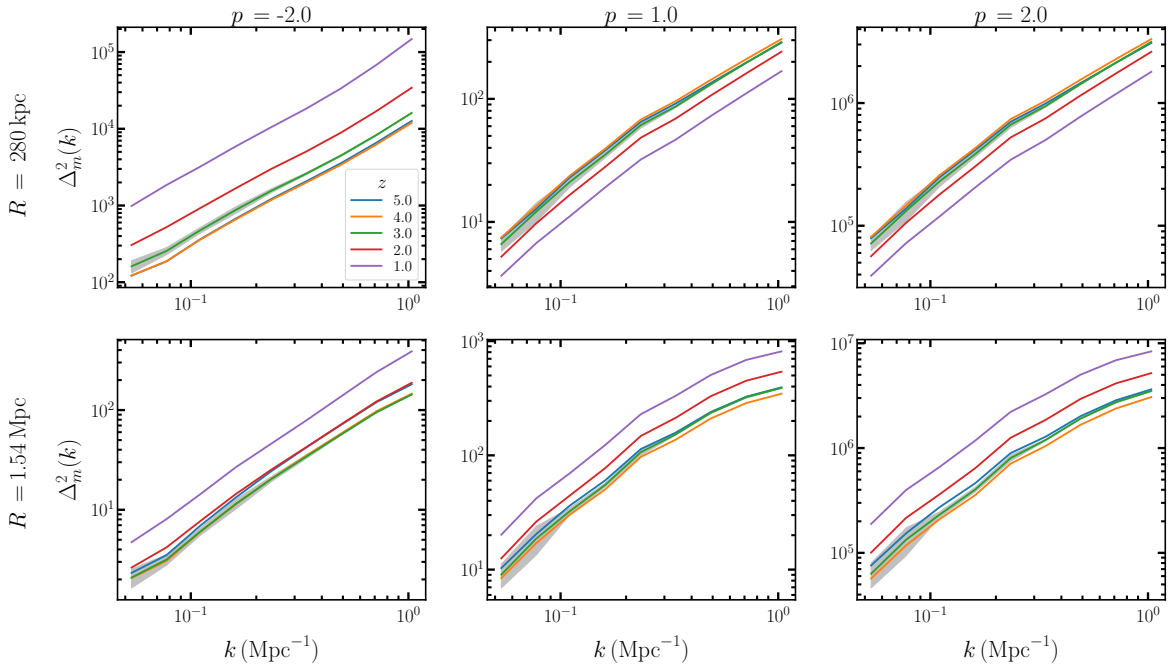


Figure 7. Marked HI power spectra (Δ_m^2) as a function of k mode at five different redshifts. Here, we consider three different p values and two different R values. The upper panels are at $R = 280$ kpc and the lower panels are at $R = 1.54$ Mpc. The three columns are at three different values of the parameter p which are p_{hd} (left-column), p_{ld1} (middle-column), and p_{ld2} (right-column). The shaded regions in each panel represent $\pm 1\sigma$ spread around the mean at $z = 3$.

280 kpc and 1.54 Mpc respectively, we find that the redshift evolution of Δ_m^2 resembles that of Δ_{HI}^2 , as expected. Δ_m^2 increases with decreasing z , shows a power-law behaviour with k and the separation between Δ_m^2 vs k lines at two successive z values (here $\Delta z = 1$) increases with decreasing z . This indicates that the amplitude of HI overdensities grows with time, and the cosmic web structures along the overdense regions become sharper. The amplitude of Δ_m^2 , however, is dependent on R and, at a fixed z , we find a smaller amplitude for $R = 1.54$ Mpc. Also, for a fixed Δz , the separation between the lines decreases as compared to that for $R = 280$ kpc. All this is expected as with increasing R , the peaks in m get smoothed out, which results in a reduced amplitude in the MPS. We shall investigate the MPS for a wide range of R in section 4.2 that can be considered to cover a wide range of 21-cm observations of the post-reionization era with different telescopes.

4.1.2 MPS for p_{ld1}

Considering the two bottom rows in Figure 6, which show the marked field with p_{ld1} , we find that the high-density peaks as in the top four rows are missing here. This is more clearly visible for $R = 1.54$ Mpc panels. The redshift evolution in the bottom two panels is mostly due to the low-density regions, exhibiting substantial evolution with redshift. Even though for different R , the marked fields visually look different, qualitatively the evolution looks similar.

In order to connect this evolution with the MPS, we now consider the middle and the right columns in Figure 7. We find that for a fixed R , the z evolution and k dependence of Δ_m^2 is similar for the two p values, only the amplitude is higher for the higher p . Here also, the separation between Δ_m^2 vs R lines at $\Delta z = 1$ increases with decreasing z . However, the trend in the z evolution changes, as we vary R , keeping the p value fixed. For $R = 280$ kpc, the amplitude of Δ_m^2 decreases with decreasing z , whereas the opposite happens for $R = 1.54$ Mpc. The shape of Δ_m^2 , (the k dependence), also changes with R . This behaviour can be understood as follows. Considering the third row of Figure 5, which shows the marked field with p_{ld1} and $R = 280$ kpc, we find that the cosmic web structures along which we see lower values of m (which correspond to the overdensities in the H I distribution) are sharp and prominent. The high m (or underdensity) regions are bounded by these webs. m attaining the peak values in these regions occupy a larger fraction of the simulation volume than the other m regions and thus they act as a nearly constant background. At the highest redshift $z = 5$, the size of these regions was smaller. However, as the redshift decreases, matter flows from low- to high-density regions, making the cosmic web structures sharper and the m regions with peak values wider. Since the regions with peaks of m act as background here, the power spectrum is dominated by the low m regions where the amplitude decreases as matter flows in with decreasing z . This can also be seen in the fifth row of Figure 6 where Δm is most prominent in the low m regions. Due to this, Δ_m^2 decreases with decreasing z for $R = 280$ kpc.

Something remarkable happens in the marked field when we use $R = 1.54$ Mpc, as shown in the last row of Figure 5. Due to the smoothing over a large scale, the low m regions spread out taking away portions from the high m regions. These low m regions are no longer sharp, rather they occupy most of the volume, squeezing the boundaries of the high m regions, and making them appear like small isolated islands. These high m islands are smaller and fewer in number at the highest redshift $z = 5$. On the other hand, the low m regions occupying a larger fraction of the simulation volume than the high m regions, appear as a background on top of which the islands are painted. The last row of Figure 6 shows that Δm is nearly zero in the low m regions, suggesting that the flow of matter from low to high density does not get captured in terms of no change in the density along the cosmic web structures is seen when the field is smoothed over a sufficiently large scale. On the other hand, Δm is in non-zero at the high m regions, indicating that the power spectrum is dominated by these regions. As the redshift decreases, the size and number of the high m regions increase, which increases Δm with decreasing z . Due to this, Δ_m^2 increases with decreasing z for $R = 1.54$ kpc.

4.2 The smoothing scale (R) dependence of the MPS

Δ_m^2 as a function of R and for $k = 0.16 \text{ Mpc}^{-1}$, which represent a sufficiently large scale, is shown in Figure 8 for halos (top panels) and H I (bottom panels) fields. The left and right panels respectively are for p_{hd} and p_{ld1} . For the clarity of presentation, we consider here only three different redshifts $z = 1, 2, \text{ and } 3$. Each line in a panel is plotted for 30 different values of R in the range 0 to 4.2 Mpc, at the step of 0.14 Mpc. At first glance, we see that the MPS shows a strong dependence on the smoothing scale R . On the other hand, the standard H I power spectra are expected to be independent of the smoothing scale as long as the smoothing

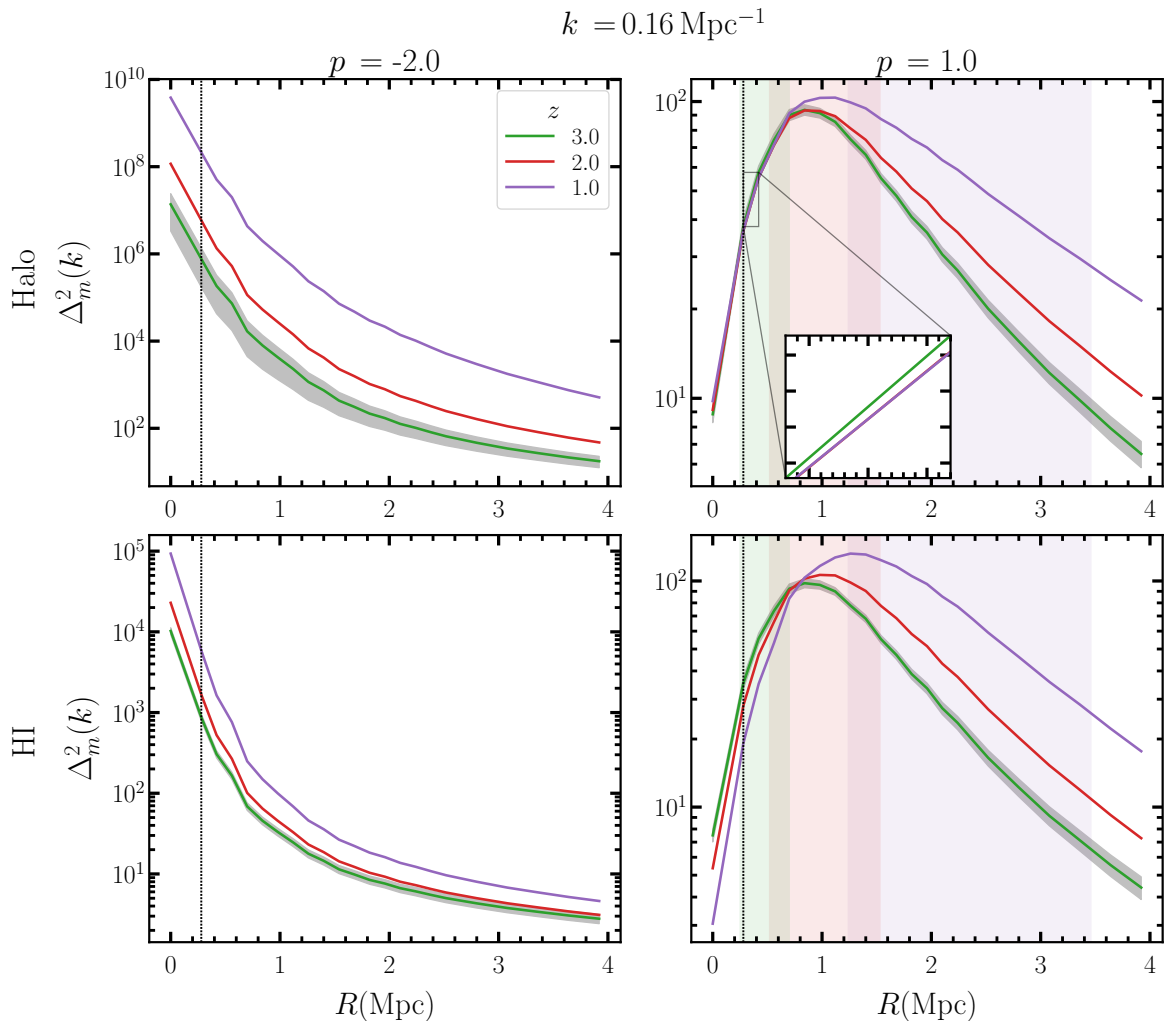


Figure 8. Δ_m^2 for halo (upper panels) and HI (lower panels) fields as a function of R for $k = 0.16 \text{ Mpc}^{-1}$ and at three different redshifts. We consider the mark parameters $\rho_* = 0.01$ and two different p values, p_{hd} (left panels) and p_{ldl} (right panels). The shaded regions around the line at $z = 3$, in each panel of the right column, represent $\pm 1\sigma$ confidence interval around the mean value. Each vertical shaded region is the range between two different R values i.e. R_{ta} (right end) and R_{c} (left end) that respectively corresponds to σ_{ta} and σ_{c} from the Λ CDM cosmology. The colour of a shaded region at a fixed z matches with the line colour at that z . The vertical dotted line is the resolution limit ($R = 280 \text{ kpc}$) of our simulation.

scale is $\lesssim 2\pi/k_f$ where k_f is the k value where the power spectrum is considered, which is 0.16 Mpc^{-1} here as mentioned above.

4.2.1 MPS for p_{hd}

Considering the left panels, we see that with p_{hd} , the shape of Δ_m^2 for HI field closely resembles that of the halo field, which is expected, as the HI distribution traces halo distribution. However, the amplitude of Δ_m^2 for HI is smaller than that of the halo field as several peaks in

m which are present in the halo distribution are missed in the H I distribution due to the H I assignment prescription in eq. 2.1. We further find that at a fixed z , the amplitude of Δ_m^2 falls exponentially with increasing R for both halo and H I fields. This is also what we expect as with the increasing R , the peaks in their marked distribution get smoothed out, which results in the reduced amplitude in Δ_m^2 . Furthermore, Δ_m^2 vs R lines at $\Delta z = 1$ are nearly parallel, but separated by a constant factor. Also, this separation increases with decreasing z . This difference for the H I field is smaller compared to that for the halo field. This also matches our expectation as the evolution in the H I overdensity is weaker than the halo overdensity.

4.2.2 MPS for p_{ld1}

In the right panels of Figure 8, Δ_m^2 for p_{ld1} , probes the clustering in the halo and H I fields due to the distribution and evolution of the matter in the low-density regions. The trend of Δ_m^2 for the H I fields matches that for the halo field. However, the features are more clearly visible in the MPS of the H I field than in the halo field for lower values of R . We now focus on Δ_m^2 for the H I field. We find that for small values of R , the amplitude of Δ_m^2 decreases with decreasing z at a fixed R . This trend gets reversed for large R values, resulting in Δ_m^2 vs R lines for different redshifts intersecting each other at a point where $R \sim 0.8$ Mpc. As we have already established in section 4.1 for $R = 280$ kpc that Δ_m^2 captures the low m (or overdensity) regions along the web structures where m decreases as the matter flows in with time (see the third row of Figure 5). This is indicated by the decreasing amplitude of Δ_m^2 with decreasing z . Therefore, for $280 \text{ kpc} \lesssim R \lesssim 0.8 \text{ Mpc}$, Δ_m^2 captures the evolving high-density regions with time along the web structures due to the flow of matter. We have also established in section 4.1 that for $R = 1.54$ Mpc, the amplitude of Δ_m^2 increases with decreasing z , and this captures the regions with high m (or lower-density) growing in size and number with time due to the flow of matter away from these regions. This flow makes nearly zero change in low m (< 1) regions for this R value. Hence, the reverse trend, seen at $R > 0.8$ Mpc where the amplitude of Δ_m^2 grows with decreasing redshift, is largely due to the growth of low-density regions.

Further, we find that for a fixed z (say $z = 1$), there is a turnover value of $R \sim 1.2$ Mpc, both sides of which the Δ_m^2 values fall. For R values smaller than this scale, the growth of Δ_m^2 is rapid. On the other hand, for $R > 1.2$ Mpc, the decline of Δ_m^2 with R is relatively shallower. As we previously discussed, the growth of Δ_m^2 with R in the range $280 \text{ kpc} \lesssim R \lesssim 0.8 \text{ Mpc}$ is decided by the evolution of the high-density regions along the cosmic web, this indicates that Δ_m^2 continues to capture this evolution till $R \sim 1.2$ Mpc. The peak R value is smaller for higher redshifts, and the distance between two successive peaks decreases with increasing z . Also, the peak Δ_m^2 value decreases with increasing z . This indicates Δ_m^2 to capture the growth of structures along the cosmic web with a faster rate at lower z than that at higher z and this growth is visible for R values below the turnover scale. However, for R values greater than the turnover scale, the evolution of the cosmic web is not visible as any change within the smoothing scale is being smoothed out, and the evolution of Δ_m^2 here is controlled by the low-density regions. The faster decline of Δ_m^2 with increasing R indicates that the average size of the low-density regions is smaller at high redshifts, therefore, any changes within those at high z can be masked easily by choosing higher R . At low redshifts, the low-density regions are relatively larger and therefore need larger R to mask out the evolution.

The above results are found to be true for other k values in the range $0.05 \leq k \leq 1.0 \text{ Mpc}^{-1}$. However, the nature of Δ_m^2 vs R curves change when a different value for ρ_* is assumed or a different negative value for p is taken. However, within a smaller range $0 < \rho_* \leq 0.1$, we find that the above results qualitatively hold.

We next investigate if the features of Δ_m^2 vs R for p_{ld1} in Figure 8 which can give more information about the growth of structures in the HI field. The linear perturbation theory predicts that the growth of the structures in the self-gravity falls in the non-linear regime when the density fluctuation $\sigma(R, z)$ inside a sphere of radius R attains a value between the turnaround and collapse values i.e., $\sigma_{\text{ta}} = 1.06$ and $\sigma_c = 1.686$ from the Λ CDM cosmology. The σ_{ta} is the fluctuation level at which the non-linear regime begins and the smoothing scale R for which the average fluctuation of the field attains this value can be designated as R_{ta} . On the other hand, at σ_c the matter for smoothing scale R_c gets collapsed to form bound objects. At each z , we plot a shaded region between two different R values that correspond to the σ_{ta} (right edge) and σ_c (left edge) in the right panels of Figure 8. The width of the shaded regions increases with decreasing z and also the shaded region shifts toward higher R with decreasing z . Considering the right-lower panel, at a fixed z , the part of Δ_m^2 vs R line falling in the shaded region probes the non-linear evolution of the HI over the R -range corresponding to the shaded region. Also, the left edge of a shaded region of a particular colour intersects Δ_m^2 vs R line of the same colour at a point. This point moves in the direction of increasing amplitude of Δ_m^2 with increasing R and with decreasing z which indicates capturing the hierarchal growth of the structures, where the small-scale structures are expected to form at high redshifts while at low redshifts larger size of structures is also expected.

5 Summary and discussions

The intensity mapping of the neutral hydrogen (HI) distribution in the post-reionization era presents a potential means to investigate the HI clustering and its evolution in this era. A number of models of HI distribution in the post-reionization era indicate that HI in this era is mostly associated with the galaxies that reside inside the dark matter halos which are sitting at the matter over-densities. That is why the 21-cm signal from this era is expected to be a cleaner probe of underlying matter clustering. However, the normal HI density power spectrum only captures the information inherent in the high densities. The information about the HI distributed at low and intermediate densities is missed in the standard HI power spectrum. Many previous studies have shown that there is almost no evolution of the HI clustering with time, indicated by the overlapping feature of its power spectrum at different redshifts over a wide range of k -modes. It is possible to perform a simple modification in the HI density field in a physically meaningful and informative way so that the power spectrum from the modified field could capture the information about HI distribution at different densities as well as its evolution with time. This modification serves as the mark and the modified field is denoted as the marked HI field. Therefore, the power spectrum extracted from the marked field is known as the marked power spectrum (MPS). This work is the first application of the MPS on the HI distribution in the post-reionization era and focuses on studying the HI clustering and its evolution at various length scales and redshifts in this era.

In this work, we rely on a semi-numerical technique to simulate the H_I density field in the redshift range $1 \leq z \leq 5$. We then apply a non-linear transformation (eq. 3.2), formulated in ref. [100], on the fields to produce the marked field m . This non-linear transformation is a function of local density only and has three free parameters. These parameters are the smoothing radius R , a threshold on the local density ρ_* , and an exponent p . The values of these parameters are chosen based on the features and length scales of interest. Therefore, by tuning the various parameters, we can extract information from various regions using MPS, as opposed to the regular H_I density power spectrum, which mostly carries information from the high-density regions. Further, since m is a non-linear function of density, MPS contains some higher-order density statistics and hence retains more information compared to the regular density power spectrum. Here, we have studied MPS for a number of different parameter combinations and compared the results with the regular density power spectrum. We have also produced different visual maps of normal and marked H_I density fields and tried to interpret the results exhibited by the power spectrum. The main findings from our analysis are:

- Our simple semi-numerical setup suggests that there is an evolution in H_I density at low and intermediate-density regions ($\rho/\bar{\rho} < 3$) that are not captured by the standard density power spectrum.
- Considering marks $m \propto [1/\rho_R]^p$, we find that for a positive p , MPS can capture the evolution of the low-density regions, whereas for a negative p the mark is sensitive to the evolution of the high-density regions similar to the standard density power spectrum. However, m with $p < -1$ tends to enhance even the slightest evolution in the high-density regions. As a result, MPS with $p < -1$ shows evolution with z , unlike the standard power spectrum. Although the results are sensitive to the choice of the smoothing radius R .
- MPS of the H_I field shows an approximate power law behaviour with k -mode at every z similar to the normal H_I power spectrum, although having a different slope. This indicates that mark fields can also be viewed as biased tracers of the underlying matter field.
- Considering our exact mark function in eq. 3.2 and for a fixed $\rho_* = 0.01$, we find that for $p = -2$, the MPS shows significant redshift evolution at all k for the smallest value of R . As R increases, the z evolution tends to become less prominent, and finally, for the highest value of R we find that MPS evolves only marginally with z . This is because, with the increasing R , we are smoothing out the density field. When R becomes comparable to the typical size of the over-dense regions, any changes happening within those will be masked out. As a result, the information about the evolution will not be fully captured by MPS.
- Now, for $p = 1$, we find that the z evolution of MPS is significant across the various R values chosen. Only the order of the evolution with z changes between small and large R , causing a cross-over point at $R \sim 0.8$ Mpc where the results for different z intersect and we find a minimum evolution of MPS around this scale. For a fixed z (say

$z = 1$), we find a turnover value around $R \sim 1.2$ Mpc. To the left of this point, MPS increases rapidly as R increases capturing the evolution of the high-density regions in the cosmic web due to the transfer of matter from low to high densities. To the right of this point, the MPS gradually declines with increasing R capturing the evolution in the low-density regions only. The typical size of the low-density regions is larger than the size of the high-density regions. As a result, the evolution in the low densities can still be captured even at the highest value of R chosen in the analysis. The size of these regions grows with decreasing z . Therefore, we expect to capture the evolution of the low-density regions at low z using MPS even if the field is heavily smoothed.

- We conclude that the evolution of H I density, driven by the flow from low- to high-density regions, can be effectively probed across different density regimes and stages by appropriately selecting the functional form and parameters of the mark. MPS may also reflect information about some higher-order statistical moments of the H I field, thereby offering a richer set of statistical insights. Finally, information about the H I content at low and intermediate densities is crucial for a correct and consistent analysis of H I content and its evolution, particularly when using the 21-cm background. MPS offers a less biased statistic for constraining parameters compared to the standard power spectrum.

This work is the first to consider the application of mark statistics on the post-reionization H I field to track the distribution and evolution of the H I content using the corresponding marked power spectra. The current analysis is preliminary as we consider only a very simple model of H I distribution where H I resides at the center of each dark matter halo and we focused mostly on one functional form of the mark, albeit with various values of the parameters. In practice, we expect the H I to be contained by galaxies that reside inside the halos. Some diffuse H I may reside outside of the galaxies as well. Not only that but H I also moves as a combination of bulk and local motions [49]. These collectively contribute to shaping the H I distribution in the post-reionization era. Furthermore, our simulation cannot resolve the H I containing halos below a certain mass of $1.09 \times 10^9 M_\odot$ at $z > 3.5$. The H I densities corresponding to these halos will likely contribute to low- and intermediate-density regimes. However, ref. [42] discussed that ignoring the smaller halos has a minor effect on the H I power spectrum even at $z \sim 6$ but may have a significant impact on MPS. We plan to use more robust simulations and address all the above issues in future work.

6 Acknowledgements

MK and MS acknowledge financial support from the foundations Carl Tryggers stiftelse för vetenskaplig forskning (grant agreement no. CTS 21:1376) and Magnus Bergvalls stiftelse (grant agreement no. 2021-04407) awarded to docent Martin Sahlén. MS also acknowledges financial support from the Swedish National Space Agency (Rymdstyrelsen) through the Senior Researcher Career grant No. 2020-00108. The simulations and statistical analysis presented in this paper have mainly used the computing resources available to the Cosmology with Statistical Inference (CSI) research group at the Indian Institute of

Technology Indore (IIT Indore). The computations and data storage were also enabled by resources provided by the National Academic Infrastructure for Supercomputing in Sweden (NAISS), partially funded by the Swedish Research Council through grant agreement no. 2022-06725. DS acknowledges the support of the Canada 150 Chairs program, the Fonds de recherche du Québec Nature et Technologies (FRQNT) and Natural Sciences and Engineering Research Council of Canada (NSERC) joint NOVA grant, and the Trottier Space Institute Postdoctoral Fellowship program. SM acknowledges financial support through the project titled ‘‘Observing the Cosmic Dawn in Multicolour using Next Generation Telescopes’’ funded by the Science and Engineering Research Board (SERB), Department of Science and Technology, Government of India through the Core Research Grant No. CRG/2021/004025.

A Appendix

A.1 A different functional form of the mark

We have already discussed in section 3 that the mark could be any arbitrary function of the property of a field. However, it is chosen according to the information in the field that we want to draw and which is not straightforward to extract from the standard distribution. Since, in this paper, we are interested in studying the H_I clustering and its evolution with time. This is why we opted for the mark as a function of local density which is smoothed over a scale R and used the formulation of ref. [100] (eq. 3.2). The major advantage of using eq. 3.2 is that this equation for $\rho_* \rightarrow 0$ scales as $m \approx [1/\rho_R]^p$ and when it is applied to a field, then the power spectrum of this field does explicitly feature the density. Another functional form of the mark as a function of local density is formulated in ref. [108] and is given by

$$m_1(\mathbf{x}, t; \rho_*, p) = \frac{[\rho(\mathbf{x}, t)]^p}{[\rho_*]^p + [\rho(\mathbf{x}, t)]^p}, \quad (\text{A.1})$$

This form was used to encode the information about which galaxies reside inside which halos. This is because the m_1 produces the marked field in the range 0 (for $\rho \ll \rho_*$) and 1 (for $\rho \gg \rho_*$) in the sense that a given position either has a galaxy or not. Hence, the marked power spectrum with m_1 does not explicitly feature a density. Note that the m_1 is the function of non-smoothed density, whereas the observable of the H_I field is expected to be related to the smoothed H_I density, which is a continuous variable and not 1 or 0. Thus, the m_1 is not informative in the sense of probing the H_I clustering and its evolution with time in the post-reionization era.

A.2 The impact of the parameter ρ_* on the marked power spectra

The figures in this paper are shown for a fixed value of the free parameter ρ_* i.e., $\rho_* = 0.01$. It is, however, imperative to look at the impact of different values of this parameter on the marked power spectrum in order to see the robustness of the results. In Figure 10, we show the marked power spectrum (Δ_m^2) at various redshifts for different values of the marked parameters ρ_* , p and R . We first consider the two left columns at $\rho_* = 0.1$ and 1.0 and with p_{ld1} . Comparing these two columns with the middle column of Figure 7, which shows Δ_m^2 for $\rho_* = 0.01$ and p_{ld1} , side by side, we see that for each smoothing scale the amplitude in

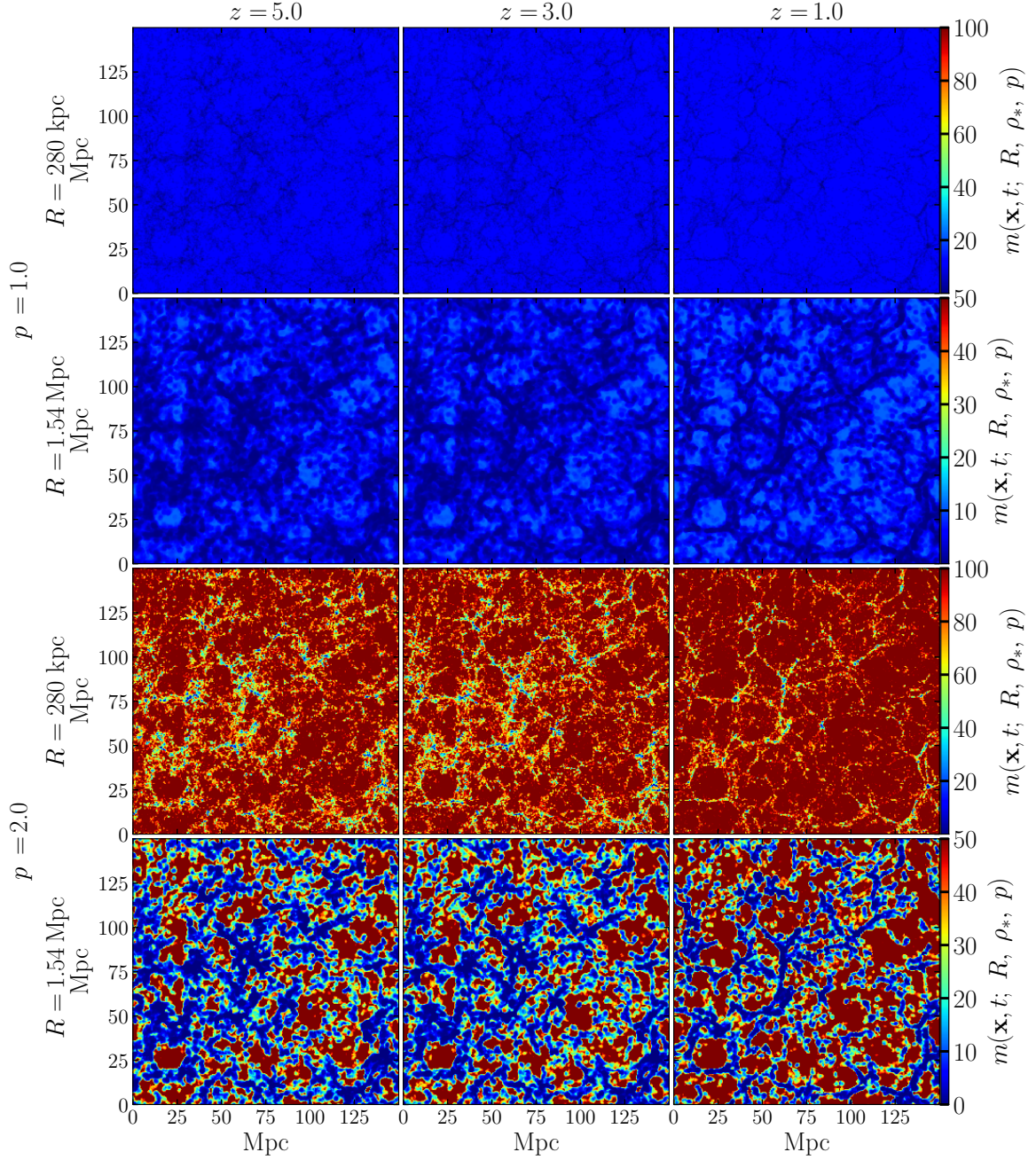


Figure 9. Marked HI field (m) at different redshifts (decreasing from left to right) and for different mark parameters (varying in the vertical direction). Here, the value of the parameter ρ_* is 0.1. The top two rows show the time evolution in m , calculated for two different R values i.e., $R = 280 \text{ kpc}$ and 1.54 Mpc as well as p_{ld1} . The bottom two rows show the same but now for p_{ld2} .

Δ_m^2 decreases with increasing ρ_* . The shape of Δ_m^2 , however, remains the same. Here also, for a fixed Δz , the separation between two Δ_m^2 vs k lines decreases with increasing ρ_* . In order to understand these behaviours, we compare the marked field in the two bottom rows

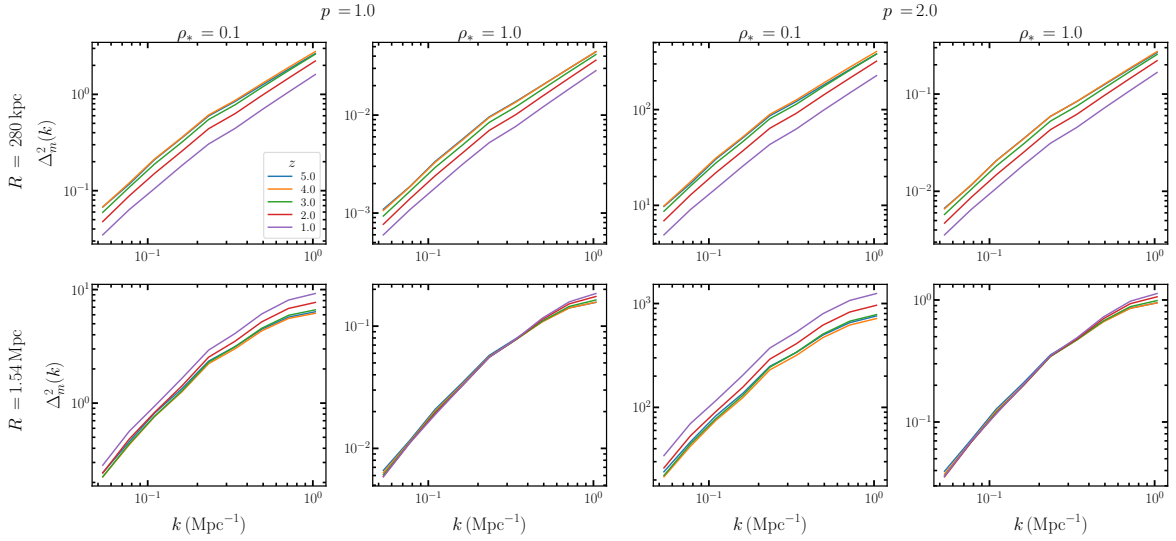


Figure 10. Marked HI power spectra (Δ_m^2) as a function of k mode at five different redshifts. The upper panels are shown at a smoothing scale of $R = 280$ kpc, whereas the lower panels are shown at $R = 1.54$ Mpc. The two left-columns are at p_{ld1} and for two different ρ_* i.e., $\rho_* = 0.1$ and 1.0 whereas the two right-columns are at p_{ld2} .

of Figure 5, which show the marked field for $\rho_* = 0.01$ and p_{ld1} , with the two top rows in Figure 9 at $\rho_* = 0.1$ and p_{ld1} . We find that with a larger value of ρ_* the marked field shows its lower amplitude as well as the decreased contrast between high and low m . Due to this, Δ_m^2 amplitude decreases with increasing ρ_* . Also, the evolution in m can not be clearly visualized in the marked field with larger ρ_* . This evolution is also not captured well statistically by Δ_m^2 .

Now, considering the two right columns in Figure 10, we find that the larger value of p (here $p = 2$) increases the amplitude of Δ_m^2 . The larger p also increases the separation between two Δ_m^2 vs k lines for a fixed Δz capturing the redshift evolution in the marked field. However, the increase in this separation is substantial for $\rho_* = 0.1$. This can be visualized in the two bottom rows in Figure 9 at $\rho_* = 0.1$ and p_{ld2} . Comparing these rows with two top rows, we see the increased amplitude in m for p_{ld2} as well as the increased contrast between high and low m . Here also, the evolution in m is visually clear which is well captured by Δ_m^2 . We thus conclude that with a small p , the small value of ρ_* is a good choice to probe the HI clustering and its evolution with time.

References

- [1] P. Madau, A. Meiksin and M.J. Rees, *21-CM tomography of the intergalactic medium at high redshift*, *Astrophys. J.* **475** (1997) 429 [[astro-ph/9608010](#)].
- [2] S. Furlanetto, S.P. Oh and F. Briggs, *Cosmology at Low Frequencies: The 21 cm Transition and the High-Redshift Universe*, *Phys. Rept.* **433** (2006) 181 [[astro-ph/0608032](#)].

- [3] S. Bharadwaj, B.B. Nath, B.B. Nath and S.K. Sethi, *Using HI to probe large scale structures at $z \sim 3$* , *J. Astrophys. Astron.* **22** (2001) 21 [[astro-ph/0003200](#)].
- [4] S. Bharadwaj and S.K. Pande, *HI fluctuations at large redshifts. 2. The signal expected for gmrt*, *J. Astrophys. Astron.* **24** (2003) 23 [[astro-ph/0307303](#)].
- [5] S. Bharadwaj and P.S. Srikant, *HI Fluctuations at Large Redshifts: III - Simulating the Signal Expected at GMRT*, *Journal of Astrophysics and Astronomy* **25** (2004) 67 [[arXiv:astro-ph/0402262](#)].
- [6] S. Bharadwaj and S.K. Sethi, *HI Fluctuations at Large Redshifts. 1. Visibility correlation*, *J. Astrophys. Astron.* **22** (2001) 293 [[astro-ph/0203269](#)].
- [7] A. Loeb and S. Wyithe, *Precise Measurement of the Cosmological Power Spectrum With a Dedicated 21cm Survey After Reionization*, *Phys. Rev. Lett.* **100** (2008) 161301 [[0801.1677](#)].
- [8] S. Wyithe and A. Loeb, *The 21cm Power Spectrum After Reionization*, *Mon. Not. Roy. Astron. Soc.* **397** (2009) 1926 [[0808.2323](#)].
- [9] T.-C. Chang, U.-L. Pen, J.B. Peterson and P. McDonald, *Baryon Acoustic Oscillation Intensity Mapping as a Test of Dark Energy*, *Phys. Rev. Lett.* **100** (2008) 091303 [[0709.3672](#)].
- [10] S. Wyithe, A. Loeb and P. Geil, *Baryonic Acoustic Oscillations in 21cm Emission: A Probe of Dark Energy out to High Redshifts*, *Mon. Not. Roy. Astron. Soc.* **383** (2008) 1195 [[0709.2955](#)].
- [11] H.-J. Seo, S. Dodelson, J. Marriner, D. McGinnis, A. Stebbins, C. Stoughton et al., *A ground-based 21cm Baryon acoustic oscillation survey*, *Astrophys. J.* **721** (2010) 164 [[0910.5007](#)].
- [12] K.W. Masui, P. McDonald and U.-L. Pen, *Near term measurements with 21 cm intensity mapping: neutral hydrogen fraction and BAO at $z < 2$* , *Phys. Rev. D* **81** (2010) 103527 [[1001.4811](#)].
- [13] S. Bharadwaj, S.K. Sethi and T.D. Saini, *Estimation of Cosmological Parameters from HI Observations of Post-reionization Epoch*, *Phys. Rev. D* **79** (2009) 083538 [[0809.0363](#)].
- [14] A. Obuljen, E. Castorina, F. Villaescusa-Navarro and M. Viel, *High-redshift post-reionization cosmology with 21cm intensity mapping*, *JCAP* **05** (2018) 004 [[1709.07893](#)].
- [15] T.G. Sarkar and S. Bharadwaj, *Predictions for BAO distance estimates from the cross-correlation of the Lyman- α forest and redshifted 21-cm emission*, *JCAP* **08** (2013) 023 [[1308.2551](#)].
- [16] I.P. Carucci, F. Villaescusa-Navarro and M. Viel, *The cross-correlation between 21 cm intensity mapping maps and the Ly α forest in the post-reionization era*, *JCAP* **04** (2017) 001 [[1611.07527](#)].
- [17] A.K. Sarkar, S. Bharadwaj and T.G. Sarkar, *Predictions for measuring the cross power spectrum of the HI 21-cm signal and the Lyman- α forest using OWFA*, *JCAP* **05** (2018) 051 [[1804.00454](#)].
- [18] F. Villaescusa-Navarro, M. Viel, D. Alonso, K.K. Datta, P. Bull and M.G. Santos, *Cross-correlating 21cm intensity maps with Lyman Break Galaxies in the post-reionization era*, *JCAP* **03** (2015) 034 [[1410.7393](#)].

- [19] T.G. Sarkar, *CMBR Weak Lensing and HI 21-cm Cross-correlation Angular Power Spectrum*, *JCAP* **02** (2010) 002 [[0908.1840](#)].
- [20] T.G. Sarkar, K.K. Datta and S. Bharadwaj, *The CMBR ISW and HI 21-cm Cross-correlation Angular Power Spectrum*, *JCAP* **08** (2009) 019 [[0810.3649](#)].
- [21] E. Abdalla et al., *The BINGO project - I. Baryon acoustic oscillations from integrated neutral gas observations*, *Astron. Astrophys.* **664** (2022) A14 [[2107.01633](#)].
- [22] A.A. Costa et al., *The BINGO project - VII. Cosmological forecasts from 21 cm intensity mapping*, *Astron. Astrophys.* **664** (2022) A20 [[2107.01639](#)].
- [23] CHIME collaboration, *An Overview of CHIME, the Canadian Hydrogen Intensity Mapping Experiment*, *Astrophys. J. Supp.* **261** (2022) 29 [[2201.07869](#)].
- [24] X. Chen, *The Tianlai project: a 21cm cosmology experiment*, *Int. J. Mod. Phys. Conf. Ser.* **12** (2012) 256 [[1212.6278](#)].
- [25] P. Jiang, Y. Yue, H. Gan, R. Yao, H. Li, G. Pan et al., *Commissioning progress of the FAST*, *Science China Physics, Mechanics, and Astronomy* **62** (2019) 959502 [[1903.06324](#)].
- [26] S. Johnston, R. Taylor, M. Bailes, N. Bartel, C. Baugh, M. Bietenholz et al., *Science with ASKAP. The Australian square-kilometre-array pathfinder*, *Experimental Astronomy* **22** (2008) 151 [[0810.5187](#)].
- [27] L.B. Newburgh, K. Bandura, M.A. Bucher, T.C. Chang, H.C. Chiang, J.F. Cliche et al., *HIRAX: a probe of dark energy and radio transients*, in *Ground-based and Airborne Telescopes VI*, H.J. Hall, R. Gilmozzi and H.K. Marshall, eds., vol. 9906 of *Society of Photo-Optical Instrumentation Engineers (SPIE) Conference Series*, p. 99065X, August, 2016, DOI [[1607.02059](#)].
- [28] K. Vanderlinde, A. Liu, B. Gaensler, D. Bond, G. Hinshaw, C. Ng et al., *The Canadian Hydrogen Observatory and Radio-transient Detector (CHORD)*, in *Canadian Long Range Plan for Astronomy and Astrophysics White Papers*, vol. 2020, p. 28, October, 2019, DOI [[1911.01777](#)].
- [29] Square Kilometre Array Cosmology Science Working Group, D.J. Bacon, R.A. Battye, P. Bull, S. Camera, P.G. Ferreira et al., *Cosmology with Phase 1 of the Square Kilometre Array Red Book 2018: Technical specifications and performance forecasts*, *Publ. Astron. Soc. Austral.* **37** (2020) e007 [[1811.02743](#)].
- [30] S. Paul, M.G. Santos, Z. Chen and L. Wolz, *A first detection of neutral hydrogen intensity mapping on Mpc scales at $z \approx 0.32$ and $z \approx 0.44$* , [2301.11943](#).
- [31] A. Ghosh, S. Bharadwaj, S.S. Ali and J.N. Chengalur, *Improved foreground removal in GMRT 610 MHz observations towards redshifted 21-cm tomography*, *Mon. Not. Roy. Astron. Soc.* **418** (2011) 2584 [[1108.3707](#)].
- [32] A. Ghosh, J. Prasad, S. Bharadwaj, S.S. Ali and J.N. Chengalur, *Characterizing foreground for redshifted 21 cm radiation: 150 MHz Giant Metrewave Radio Telescope observations*, *Mon. Not. Roy. Astron. Soc.* **426** (2012) 3295 [[1208.1617](#)].
- [33] E.R. Switzer, K.W. Masui, K. Bandura, L.M. Calin, T.C. Chang, X.L. Chen et al., *Determination of $z \sim 0.8$ neutral hydrogen fluctuations using the 21cm intensity mapping autocorrelation.*, *Mon. Not. Roy. Astron. Soc.* **434** (2013) L46 [[1304.3712](#)].

- [34] P. Bull, P.G. Ferreira, P. Patel and M.G. Santos, *Late-time Cosmology with 21 cm Intensity Mapping Experiments*, *Astrophys. J.* **803** (2015) 21 [1405.1452].
- [35] A.K. Sarkar, S. Bharadwaj and S.S. Ali, *Fisher Matrix-based Predictions for Measuring the $z = 3.35$ Binned 21-cm Power Spectrum using the Ooty Wide Field Array (OWFA)*, *Journal of Astrophysics and Astronomy* **38** (2017) 14 [1703.00634].
- [36] F. Marin, N.Y. Gnedin, H.-J. Seo and A. Vallinotto, *Modeling The Large Scale Bias of Neutral Hydrogen*, *Astrophys. J.* **718** (2010) 972 [0911.0041].
- [37] H. Padmanabhan, A. Refregier and A. Amara, *A halo model for cosmological neutral hydrogen : abundances and clustering*, *Mon. Not. Roy. Astron. Soc.* **469** (2017) 2323 [1611.06235].
- [38] A. Pénin, O. Umeh and M. Santos, *A scale dependent bias on linear scales: the case for HI intensity mapping at $z=1$* , *Mon. Not. Roy. Astron. Soc.* **473** (2018) 4297 [1706.08763].
- [39] J.S. Bagla, N. Khandai and K.K. Datta, *HI as a probe of the large-scale structure in the post-reionization universe*, *Monthly Notices of the Royal Astronomical Society* **407** (2010) 567 [<https://academic.oup.com/mnras/article-pdf/407/1/567/3087523/mnras0407-0567.pdf>].
- [40] N. Khandai, S.K. Sethi, T. Di Matteo, R.A.C. Croft, V. Springel, A. Jana et al., *Detecting neutral hydrogen in emission at redshift $z \sim 1$* , *Mon. Not. Roy. Astron. Soc.* **415** (2011) 2580 [1012.1880].
- [41] T. Guha Sarkar, S. Mitra, S. Majumdar and T.R. Choudhury, *Constraining large-scale HI bias using redshifted 21-cm signal from the post-reionization epoch*, *Mon. Not. Roy. Astron. Soc.* **421** (2012) 3570 [1109.5552].
- [42] D. Sarkar, S. Bharadwaj and S. Ananthpindika, *Modelling the post-reionization neutral hydrogen (HI) bias*, *Mon. Not. Roy. Astron. Soc.* **460** (2016) 4310 [1605.02963].
- [43] D. Sarkar and S. Bharadwaj, *Modelling redshift space distortion in the post-reionization HI 21-cm power spectrum*, *Mon. Not. Roy. Astron. Soc.* **476** (2018) 96 [1801.07868].
- [44] D. Sarkar and S. Bharadwaj, *Redshift-space distortions of the HI 21-cm intensity mapping signal due to the internal motions within galaxies*, *Mon. Not. Roy. Astron. Soc.* **487** (2019) 5666 [1906.07032].
- [45] S. Seehars, A. Paranjape, A. Witzemann, A. Refregier, A. Amara and J. Akeret, *Simulating the large-scale structure of HI intensity maps*, *JCAP* **2016** (2016) 001 [1509.01589].
- [46] C. Modi, E. Castorina, Y. Feng and M. White, *Intensity mapping with neutral hydrogen and the Hidden Valley simulations*, *JCAP* **09** (2019) 024 [1904.11923].
- [47] R. Davé, N. Katz, B.D. Oppenheimer, J.A. Kollmeier and D.H. Weinberg, *The Neutral Hydrogen Content of Galaxies in Cosmological Hydrodynamic Simulations*, *Mon. Not. Roy. Astron. Soc.* **434** (2013) 2645 [1302.3631].
- [48] F. Villaescusa-Navarro, M. Viel, K.K. Datta and T.R. Choudhury, *Modeling the neutral hydrogen distribution in the post-reionization Universe: intensity mapping*, *JCAP* **09** (2014) 050 [1405.6713].
- [49] F. Villaescusa-Navarro et al., *Ingredients for 21 cm Intensity Mapping*, *Astrophys. J.* **866** (2018) 135 [1804.09180].

- [50] A. Rahmati, A.P. Pawlik, M. Raicevic and J. Schaye, *On the evolution of the HI column density distribution in cosmological simulations*, *Mon. Not. Roy. Astron. Soc.* **430** (2013) 2427 [[1210.7808](#)].
- [51] D. Nelson et al., *The IllustrisTNG simulations: public data release*, *Comput. Astrophys. Cosmol.* **6** (2019) 2 [[1812.05609](#)].
- [52] D. Baumann, *Inflation*, in *Theoretical Advanced Study Institute in Elementary Particle Physics: Physics of the Large and the Small*, pp. 523–686, 2011, DOI [[0907.5424](#)].
- [53] J.N. Fry, *The Galaxy correlation hierarchy in perturbation theory*, *Astrophys. J.* **279** (1984) 499.
- [54] F. Oppizzi, M. Liguori, A. Renzi, F. Arroja and N. Bartolo, *CMB constraints on running non-Gaussianity*, *JCAP* **05** (2018) 045 [[1711.08286](#)].
- [55] P. Gagrani and L. Samushia, *Information Content of the Angular Multipoles of Redshift-Space Galaxy Bispectrum*, *Mon. Not. Roy. Astron. Soc.* **467** (2017) 928 [[1610.03488](#)].
- [56] S. Bharadwaj, A. Mazumdar and D. Sarkar, *Quantifying the Redshift Space Distortion of the Bispectrum I: Primordial Non-Gaussianity*, *Mon. Not. Roy. Astron. Soc.* **493** (2020) 594 [[2001.10243](#)].
- [57] A. Mazumdar, S. Bharadwaj and D. Sarkar, *Quantifying the Redshift Space Distortion of the Bispectrum II: Induced Non-Gaussianity at Second Order Perturbation*, *Mon. Not. Roy. Astron. Soc.* **498** (2020) 3975 [[2005.07066](#)].
- [58] A. Mazumdar, D. Sarkar and S. Bharadwaj, *Quantifying the redshift space distortion of the bispectrum III : detection prospects of the multipole moments*, *Mon. Not. Roy. Astron. Soc.* **520** (2023) 2534 [[2209.03233](#)].
- [59] J. Byun and E. Krause, *Modal compression of the redshift-space galaxy bispectrum*, *Mon. Not. Roy. Astron. Soc.* (2022) [[2205.04579](#)].
- [60] M.M. Ivanov, O.H.E. Philcox, G. Cabass, T. Nishimichi, M. Simonović and M. Zaldarriaga, *Cosmology with the galaxy bispectrum multipoles: Optimal estimation and application to BOSS data*, *Phys. Rev.* **107** (2023) 083515 [[2302.04414](#)].
- [61] G. D’Amico, Y. Donath, M. Lewandowski, L. Senatore and P. Zhang, *The BOSS bispectrum analysis at one loop from the Effective Field Theory of Large-Scale Structure*, *JCAP* **2024** (2024) 059 [[2206.08327](#)].
- [62] S. Singh Gill and S. Bharadwaj, *A Brisk Estimator for the Angular Multipoles (BEAM) of the redshift space bispectrum*, *arXiv e-prints* (2024) arXiv:2405.14513 [[2405.14513](#)].
- [63] D. Sarkar, S. Majumdar and S. Bharadwaj, *Modelling the post-reionization neutral hydrogen (HI) 21-cm bispectrum*, *Mon. Not. Roy. Astron. Soc.* **490** (2019) 2880 [[1907.01819](#)].
- [64] S. Majumdar, J.R. Pritchard, R. Mondal, C.A. Watkinson, S. Bharadwaj and G. Mellema, *Quantifying the non-Gaussianity in the EoR 21-cm signal through bispectrum*, *Mon. Not. Roy. Astron. Soc.* **476** (2018) 4007 [[1708.08458](#)].
- [65] S. Bharadwaj and S.K. Pandey, *Probing non-Gaussian features in the HI distribution at the epoch of re-ionization*, *Mon. Not. Roy. Astron. Soc.* **358** (2005) 968 [[astro-ph/0410581](#)].
- [66] A.K. Shaw, S. Bharadwaj and R. Mondal, *The impact of non-Gaussianity on the Epoch of*

- Reionization parameter forecast using 21-cm power spectrum measurements*, *Mon. Not. Roy. Astron. Soc.* **498** (2020) 1480 [2005.06535].
- [67] A.K. Shaw, S. Bharadwaj, D. Sarkar, A. Mazumdar, S. Singh and S. Majumdar, *A fast estimator for quantifying the shape dependence of the 3D bispectrum*, *JCAP* **12** (2021) 024 [2107.14564].
- [68] A. Nandi, S.S. Gill, D. Sarkar, A.K. Shaw, B. Pandey and S. Bharadwaj, *The size and shape dependence of the SDSS galaxy bispectrum*, *New Astron.* **113** (2024) 102292 [2401.15958].
- [69] V. Gluscevic and R. Barkana, *Statistics of 21-cm fluctuations in cosmic reionization simulations: PDFs and difference PDFs*, *Mon. Not. Roy. Astron. Soc.* **408** (2010) 2373 [1005.3814].
- [70] S. Yoshiura, H. Shimabukuro, K. Takahashi and T. Matsubara, *Studying topological structure of 21-cm line fluctuations with 3D Minkowski functionals before reionization*, *Mon. Not. Roy. Astron. Soc.* **465** (2017) 394 [1602.02351].
- [71] A. Aviles, K. Koyama, J.L. Cervantes-Cota, H.A. Winther and B. Li, *Marked correlation functions in perturbation theory*, *JCAP* **01** (2020) 006 [1911.06362].
- [72] M. Kärcher, J. Bel and S. de la Torre, *Towards an optimal marked correlation function analysis for the detection of modified gravity*, **2406.02504**.
- [73] M. White, *A marked correlation function for constraining modified gravity models*, *JCAP* **11** (2016) 057 [1609.08632].
- [74] S. Satpathy, R.A.C. Croft, S. Ho and B. Li, *Measurement of marked correlation functions in SDSS-III Baryon Oscillation Spectroscopic Survey using LOWZ galaxies in Data Release 12*, *Mon. Not. Roy. Astron. Soc.* **484** (2019) 2148 [1901.01447].
- [75] N.H.M. Crighton et al., *The neutral hydrogen cosmological mass density at $z = 5$* , *Mon. Not. Roy. Astron. Soc.* **452** (2015) 217 [1506.02037].
- [76] E. Massara, F. Villaescusa-Navarro, S. Ho, N. Dalal and D.N. Spergel, *Using the marked power spectrum to detect the signature of neutrinos in large-scale structure*, *Phys. Rev. Lett.* **126** (2021) 011301.
- [77] E. Massara, F. Villaescusa-Navarro, C. Hahn, M.M. Abidi, M. Eickenberg, S. Ho et al., *Cosmological information in the marked power spectrum of the galaxy field*, *The Astrophysical Journal* **951** (2023) 70.
- [78] M.C. Neyrinck, I. Szapudi and A.S. Szalay, *Rejuvenating the Matter Power Spectrum: Restoring Information with a Logarithmic Density Mapping*, *Astrophys. J.* **698** (2009) L90 [0903.4693].
- [79] M.C. Neyrinck, I. Szapudi and A.S. Szalay, *Rejuvenating Power Spectra. II. The Gaussianized Galaxy Density Field*, *Astrophys. J.* **731** (2011) 116 [1009.5680].
- [80] Planck Collaboration, P.A.R. Ade, N. Aghanim, C. Armitage-Caplan, M. Arnaud, M. Ashdown et al., *Planck 2013 results. XVI. Cosmological parameters*, *Astron. Astrophys.* **571** (2014) A16 [1303.5076].
- [81] R. Mondal, S. Bharadwaj, S. Majumdar, A. Bera and A. Acharyya, *The effect of non-Gaussianity on error predictions for the Epoch of Reionization (EoR) 21-cm power spectrum*, *Mon. Not. Roy. Astron. Soc.* **449** (2015) L41 [1409.4420].

- [82] D.J. Eisenstein and W. Hu, *Power Spectra for Cold Dark Matter and Its Variants*, *Astrophys. J.* **511** (1999) 5 [[astro-ph/9710252](#)].
- [83] Y.B. Zel'dovich, *Gravitational instability: An approximate theory for large density perturbations.*, *Astron. Astrophys.* **5** (1970) 84.
- [84] M. Davis, G. Efstathiou, C.S. Frenk and S.D.M. White, *The evolution of large-scale structure in a universe dominated by cold dark matter*, *Astrophys. J.* **292** (1985) 371.
- [85] A. Jenkins, C.S. Frenk, S.D.M. White, J.M. Colberg, S. Cole, A.E. Evrard et al., *The mass function of dark matter haloes*, *Mon. Not. Roy. Astron. Soc.* **321** (2001) 372 [[arXiv:astro-ph/0005260](#)].
- [86] R.K. Sheth and G. Tormen, *An excursion set model of hierarchical clustering: ellipsoidal collapse and the moving barrier*, *Mon. Not. Roy. Astron. Soc.* **329** (2002) 61 [[arXiv:astro-ph/0105113](#)].
- [87] A.M. Wolfe, E. Gawiser and J.X. Prochaska, *Damped Ly α Systems*, *Ann. Rev. Astron. Astrophys.* **43** (2005) 861 [[astro-ph/0509481](#)].
- [88] T. Quinn, N. Katz and G. Efstathiou, *Photoionization and the formation of dwarf galaxies*, *Monthly Notices of the Royal Astronomical Society* **278** (1996) L49.
- [89] M. Dijkstra, Z. Haiman, M.J. Rees and D.H. Weinberg, *Photoionization feedback in low-mass galaxies at high redshift*, *The Astrophysical Journal* **601** (2004) 666.
- [90] A.R. Duffy, S.T. Kay, R.A. Battye, C.M. Booth, C. Dalla Vecchia and J. Schaye, *Modelling neutral hydrogen in galaxies using cosmological hydrodynamical simulations*, *Mon. Not. Roy. Astron. Soc.* **420** (2012) 2799 [[1107.3720](#)].
- [91] A. Pontzen, F. Governato, M. Pettini, C. Booth, G. Stinson, J. Wadsley et al., *Damped Lyman α systems in galaxy formation simulations*, *Monthly Notices of the Royal Astronomical Society* **390** (2008) 1349.
- [92] R. Davé, N. Katz, B.D. Oppenheimer, J.A. Kollmeier and D.H. Weinberg, *The neutral hydrogen content of galaxies in cosmological hydrodynamic simulations*, *Mon. Not. Roy. Astron. Soc.* **434** (2013) 2645 [[1302.3631](#)].
- [93] S.M. Rao, D.A. Turnshek and D.B. Nestor, *Damped Ly α Systems at $z \gtrsim 1.65$: The Expanded Sloan Digital Sky Survey Hubble Space Telescope Sample*, *Astrophys. J.* **636** (2006) 610 [[astro-ph/0509469](#)].
- [94] P. Noterdaeme, P. Petitjean, W. Carithers, I. Pâris, A. Font-Ribera, S. Bailey et al., *Column density distribution and cosmological mass density of neutral gas: Sloan digital sky survey-iii data release 9*, *Astronomy & Astrophysics* **547** (2012) L1.
- [95] N.H.M. Crighton, M.T. Murphy, J.X. Prochaska, G. Worseck, M. Rafelski, G.D. Becker et al., *The neutral hydrogen cosmological mass density at $z = 5$* , *Mon. Not. Roy. Astron. Soc.* **452** (2015) 217 [[1506.02037](#)].
- [96] T.Y. Li, R.H. Wechsler, K. Devaraj and S.E. Church, *Connecting CO Intensity Mapping to Molecular Gas and Star Formation in the Epoch of Galaxy Assembly*, *Astrophys. J.* **817** (2016) 169 [[1503.08833](#)].
- [97] S. Yang, G. Popping, R.S. Somerville, A.R. Pullen, P.C. Breyse and A.S. Maniyar, *An Empirical Representation of a Physical Model for the ISM [C II], CO, and [C I] Emission at Redshift $1 \leq z \leq 9$* , *Astrophys. J.* **929** (2022) 140 [[2108.07716](#)].

- [98] E. Schaan and M. White, *Multi-tracer intensity mapping: cross-correlations, line noise & decorrelation*, *JCAP* **2021** (2021) 068 [2103.01964].
- [99] R.K. Sheth, A.J. Connolly and R. Skibba, *Marked correlations in galaxy formation models*, *arXiv e-prints* (2005) astro [astro-ph/0511773].
- [100] M. White, *A marked correlation function for constraining modified gravity models*, *Journal of Cosmology and Astroparticle Physics* **2016** (2016) 057.
- [101] D. Stoyan, *On Correlations of Marked Point Processes*, *Mathematische Nachrichten* **116** (1984) 197.
- [102] R.A. Skibba, K.L. Masters, R.C. Nichol, I. Zehavi, B. Hoyle, E.M. Edmondson et al., *Galaxy Zoo: the environmental dependence of bars and bulges in disc galaxies*, *Mon. Not. Roy. Astron. Soc.* **423** (2012) 1485 [1111.0969].
- [103] C. Beisbart and M. Kerscher, *Luminosity- and Morphology-dependent Clustering of Galaxies*, *Astrophys. J.* **545** (2000) 6 [astro-ph/0003358].
- [104] C. Beisbart, M. Kerscher and K. Mecke, *Mark Correlations: Relating Physical Properties to Spatial Distributions*, in *Morphology of Condensed Matter*, K. Mecke and D. Stoyan, eds., vol. 600, pp. 358–390 (2002), DOI.
- [105] R. Skibba, R.K. Sheth, A.J. Connolly and R. Scranton, *The luminosity-weighted or ‘marked’ correlation function*, *Mon. Not. Roy. Astron. Soc.* **369** (2006) 68 [astro-ph/0512463].
- [106] S. Gottlöber, M. Kerscher, A.V. Kravtsov, A. Faltenbacher, A. Klypin and V. Müller, *Spatial distribution of galactic halos and their merger histories*, *Astron. Astrophys.* **387** (2002) 778 [astro-ph/0203148].
- [107] R.K. Sheth, *The halo-model description of marked statistics*, *Mon. Not. Roy. Astron. Soc.* **364** (2005) 796 [astro-ph/0511772].
- [108] M. White and N. Padmanabhan, *Breaking halo occupation degeneracies with marked statistics*, *Monthly Notices of the Royal Astronomical Society* **395** (2009) 2381 [<https://academic.oup.com/mnras/article-pdf/395/4/2381/2943841/mnras0395-2381.pdf>].
- [109] G.-B. Zhao, B. Li and K. Koyama, *Testing gravity using the environmental dependence of dark matter halos*, *Phys. Rev. Lett.* **107** (2011) 071303.
- [110] H.A. Winther, D.F. Mota and B. Li, *Environment dependence of dark matter halos in symmetron modified gravity*, *The Astrophysical Journal* **756** (2012) 166.
- [111] L. Lombriser, F. Simpson and A. Mead, *Unscreening modified gravity in the matter power spectrum*, *Phys. Rev. Lett.* **114** (2015) 251101.
- [112] D. Shi, B. Li and J. Han, *Environmental screening of dark matter haloes in $f(R)$ gravity*, *Monthly Notices of the Royal Astronomical Society* **469** (2017) 705 [https://academic.oup.com/mnras/article-pdf/469/1/705/49203330/mnras_469_1_705.pdf].
- [113] J. Armijo, Y.-C. Cai, N. Padilla, B. Li and J.A. Peacock, *Testing modified gravity using a marked correlation function*, *Monthly Notices of the Royal Astronomical Society* **478** (2018) 3627 [<https://academic.oup.com/mnras/article-pdf/478/3/3627/25072375/sty1335.pdf>].
- [114] G. Valogiannis and R. Bean, *Beyond δ : Tailoring marked statistics to reveal modified gravity*, *Phys. Rev. D* **97** (2018) 023535.

- [115] S. Satpathy, R. A C Croft, S. Ho and B. Li, *Measurement of marked correlation functions in SDSS-III Baryon Oscillation Spectroscopic Survey using LOWZ galaxies in Data Release 12*, *Monthly Notices of the Royal Astronomical Society* **484** (2019) 2148 [<https://academic.oup.com/mnras/article-pdf/484/2/2148/27620577/stz009.pdf>].
- [116] C. Hernández-Aguayo, J. Hou, B. Li, C.M. Baugh and A.G. Sánchez, *Large-scale redshift space distortions in modified gravity theories*, *Mon. Not. Roy. Astron. Soc.* **485** (2019) 2194 [[1811.09197](https://doi.org/10.1093/mnras/stz009)].
- [117] J. Armijo, C.M. Baugh, P. Norberg and N.D. Padilla, *A new marked correlation function scheme for testing gravity*, *arXiv e-prints* (2023) [arXiv:2304.06218](https://arxiv.org/abs/2304.06218) [[2304.06218](https://arxiv.org/abs/2304.06218)].